

REPORT DOCUMENTATION PAGE				Form Approved OMB No. 0704-0188	
Public reporting burden for this collection of information is estimated to average 1 hour per response, including the time for reviewing instructions, searching existing data sources, gathering and maintaining the data needed, and completing and reviewing this collection of information. Send comments regarding this burden estimate or any other aspect of this collection of information, including suggestions for reducing this burden to Department of Defense, Washington Headquarters Services, Directorate for Information Operations and Reports (0704-0188), 1215 Jefferson Davis Highway, Suite 1204, Arlington, VA 22202-4302. Respondents should be aware that notwithstanding any other provision of law, no person shall be subject to any penalty for failing to comply with a collection of information if it does not display a currently valid OMB control number. PLEASE DO NOT RETURN YOUR FORM TO THE ABOVE ADDRESS.					
1. REPORT DATE (DD-MM-YYYY) 16-01-2012		2. REPORT TYPE Final Report		3. DATES COVERED (From - To) 01/05/2009 - 31/08/2012	
4. TITLE AND SUBTITLE Experimental Investigations on Beamed Energy Aerospace Propulsion				5a. CONTRACT NUMBER FA9550-08-1-0310	
				5b. GRANT NUMBER FA9550-08-1-0310	
				5c. PROGRAM ELEMENT NUMBER	
6. AUTHOR(S) Marco Antonio Sala Minucci; Paulo Gilberto de Paula Toro; and Israel Irone Salvador				5d. PROJECT NUMBER	
				5e. TASK NUMBER	
				5f. WORK UNIT NUMBER	
7. PERFORMING ORGANIZATION NAME(S) AND ADDRESS(ES) Instituto de Estudos Avançados Rodovia dos Tamoios km 5.5 12228-001 S. J. Campos SP BRAZIL				8. PERFORMING ORGANIZATION REPORT NUMBER	
9. SPONSORING / MONITORING AGENCY NAME(S) AND ADDRESS(ES) AFOSR / IO 875 N Randolph St Arlington, VA 22203				10. SPONSOR/MONITOR'S ACRONYM(S)	
				11. SPONSOR/MONITOR'S REPORT NUMBER(S) AFRL-OSR-VA-TR-2012-1192	
12. DISTRIBUTION / AVAILABILITY STATEMENT Distribution A: Approved for Public Release					
13. SUPPLEMENTARY NOTES					
<p>14. ABSTRACT: The Laser Propulsion (LP) experiments employed the T3 Hypersonic Shock Tunnel (HST), integrated with twin gigawatt pulsed Lumonics 620-TEA CO₂ lasers to produce the required test conditions. This effort was carried out at nominal Mach numbers ranging from 6 to 10. Time-dependent surface pressure distributions were recorded together with schlieren movies of the flow field structure resulting from the laser energy deposition. These visualizations of inlet and absorption chamber flowfields enabled the qualitative analysis of important phenomena impacting laser-propelled hypersonic air-breathing flight. The data indicated laser-induced pressure increases of 0.7- 0.9 bar with laser pulse energies of ~170 J, on off-shroud induced breakdown condition, and free stream Mach number of 6. The results of this research corroborate the feasibility of laser powered, air-breathing flight with infinite specific impulse ($I_{sp}=\infty$).</p>					
15. SUBJECT TERMS					
16. SECURITY CLASSIFICATION OF:			17. LIMITATION OF ABSTRACT	18. NUMBER OF PAGES	19a. NAME OF RESPONSIBLE PERSON Marco A S Minucci
a. REPORT	b. ABSTRACT	c. THIS PAGE			19b. TELEPHONE NUMBER (include area code) +55 12 39475670

EXPERIMENTAL INVESTIGATIONS ON BEAMED ENERGY AEROSPACE PROPULSION

Marco Antonio Sala Minucci, Ph.D.
Colonel, Brazilian Air Force
Director
Principal Investigator

Paulo Gilberto de Paula Toro, Ph.D.
Laboratory Head
Co-Principal Investigator

Israel Irone Salvador, M.Sc.
Ph.D Student
Co-Principal Investigator

Instituto de Estudos Avançados
(Institute for Advanced Studies)
Rodovia dos Tamoios, Km 5,5
12228-001 São José dos Campos SP

BRAZIL

AFOSR Grant No. FA9550-08-1-0310

January 2012

2. OBJECTIVES: The research campaign covered herein is focused on the experimental analysis of the feasibility for impulse generation with a two-dimensional, repetitively-pulsed air-breathing laser Lightcraft model at hypersonic speeds. The future application of interest for this basic research endeavor is the laser launch of nano- and micro-satellites (i.e., 1-100 kg payloads) into Low-Earth-Orbit, at low-cost and on-demand. This research began with an international collaboration on Beamed Energy Propulsion between the United States Air Force and Brazilian Air Force to conduct experiments at the Prof Henry T. Nagamatsu Laboratory of Aerothermodynamics and Hypersonics (HTN-LAH).

3. STATUS OF EFFORT: The Laser Propulsion (LP) experiments employed the T3 Hypersonic Shock Tunnel (HST), integrated with twin gigawatt pulsed Lumonics 620-TEA CO₂ lasers to produce the required test conditions. This hypersonic campaign was carried out at nominal Mach numbers ranging from 6 to 10. Time-dependent surface pressure distributions were recorded together with schlieren movies of the flow field structure resulting from the laser energy deposition. These visualizations of inlet and absorption chamber flowfields, enabled the qualitative analysis of important phenomena impacting laser-propelled hypersonic air-breathing flight. The laser-induced breakdown took an elongated vertically-oriented geometry, occurring off-surface and across the inlet's mid-channel differently from static cases in which the energy was deposited very near the shroud under-surface region. The data indicated laser-induced pressure increases of 0.7- 0.9 bar with laser pulse energies of ~170 J, on off-shroud induced breakdown condition, and free stream Mach number of 6. The results of this research corroborate the feasibility of laser powered, air-breathing flight with infinite specific impulse ($I_{sp}=\infty$): i.e., without the need for propellant injection at the laser focus. Additionally, it is shown that further reductions in inlet air working fluid velocity—with attendant increases in static pressure and density—is necessary to generate higher absorption chamber pressure and engine impulse.

4. ACCOMPLISHMENTS: This Laser Propulsion experimental setup involved a Hypersonic Shock Tunnel (HST), one CO₂ laser, a 2-D cross-sectional LightCraft model, and requisite instrumentation/data acquisition system. Accurate triggering of all events was mandatory since the entire HST test window was typically ~3.0 ms depending on the desired HST flow condition, whereas the laser energy deposition time (~1 μ s) and subsequent blast wave expansion (~200 μ s) were substantially shorter. A description of the experimental setup is given below.

A. Hypersonic Shock Tunnel (HST)

During this campaign, the T3 HST facility at the Henry T. Nagamatsu Laboratory for Aerothermodynamics and Hypersonic (HTN - LAH) was used to generate the hypersonic flow over a 2-D LightCraft model. The T3 tunnel enables test section flow conditions varying from low to high enthalpies, simulating Mach numbers from approximately 6 up to 15, by replacing the nozzle throat and exit sections and varying the driver section pressure and gas composition (i.e., dry air for low enthalpy runs, and helium for higher enthalpies). For this particular HST, test times vary from 2 to 10 ms, with longer test times for lower Mach numbers. The tunnel can generate flows with enthalpies up to 10 MJ/kg, with reservoir pressures up to 25 MPa, which leads to stagnation pressures up to 200 atm and stagnation temperatures up to 7500 K in the test section.



Fig. 1 View of the T3 HST

This tunnel is composed of a 4.08 m long driver section that can operate at pressures up to 35 MPa (5000 psi, 345 bar), even though in the present experiment most test runs were performed with 3000 psi of filling pressure. A double diaphragm section (DDS) is placed between the driver and driven sections. The DDS houses four solenoid valves and the stainless steel diaphragms that control the exact moment of the experiment initiation; a third diaphragm can be used to operate the tunnel in the Gaseous Piston mode if required. This DDS section is usually filled at half of the driver's pressure and once this section is rapidly vented by activating the solenoid valves, the higher differential pressure forces the rupture of both diaphragms and hence, the onset of HST operation. Argon was selected for DDS working fluid since it is an inert gas with high molecular weight, which helps to prevent gas diffusion between the (Helium/Air) contact surface, also called interface, formed after the diaphragms burst.

A contraction region is placed just downstream of the DDS which reduces the diameter of the driver section to match that of the driven, reduced from 190.5 mm to 127 mm; this produces a stronger shock wave than the same driver-to-driven pressure ratio could produce in a comparable constant-area shock tube.

The driven section is 10.5 m long with 127 mm internal diameter, and its downstream nozzle-end is strengthened to serve as a “reservoir” for the high pressure reflected region, when operated in the reflected mode. Instrumentation ports are distributed along the entire length of the tunnel to accommodate all diagnostics required for a given experiment. In the present work, this section was fitted with three pressure transducers, two of which were separated 400 mm apart and used to measure the incoming shock wave speed. The third pressure transducer, installed at the end section close to the diverging nozzle entrance, was used to measure the reservoir pressure as well as to trigger the remaining test equipment, including the Cordin high speed digital camera, the Lumonics 622 CO₂ laser, and the data acquisition system. Installed at the downstream end of the driven section is an aluminum diaphragm that separates this section from the evacuated dump tank. Upon the arrival of the incident shock wave, this diaphragm breaks from the sudden pressure increase, and releases the shock-compressed test gas into the nozzle section.

The convergent-divergent nozzle section comprises a replaceable “throat” insert and 15° half-angle, multi-section conical nozzle. For most experiments performed in the present research, the last nozzle section was removed to decrease the standard 610 mm exit diameter (which gives an ideal Mach number of 10.0), down to 491.0 mm for an ideal Mach number of 9.12. The nozzle resides inside an evacuated, two-segment dump tank; the hypersonic flow exits into a horizontal 1.8 m diameter by 1.26 m long segment (containing the test section), joined to a vertical segment measuring 1.89 m diameter by 4.35 m tall. The test section is fitted with a horizontal hollow sting mount (designed to support test models) that also provides a 20 cm (clear-aperture) beam tube for laser beam injection. An anodized aluminum infra-red (IR) window mount had to be designed, constructed, and installed onto the external end of this hollow sting (see **Fig. 2**), and fitted with a 2 inch thick NaCl window.



Fig. 2 Hollow HST sting with IR window and mount installed.

The test section/dump tank is equipped with four orthogonally-placed ports with 50 cm aperture for optical diagnosis and instrumentation feed-thru, with the top and bottom ports being strong enough to support heavy models. In the present experiments the test section side ports were fitted with 30 cm quartz windows for schlieren photographs.

The turnaround time for the experiments performed at the T3 facility is approximately 6 hours, including: a) replacement of used diaphragms at DDS and nozzle sections, b) purge of the residual gases, c) refill of driver and driven sections with new ‘gas loads’, and d) vacuum purge of the test section dump tank. Future improvements to this facility will greatly reduce this turnaround time, allowing multiple experiments in a single day.

B. Lumonics TEA-620 Lasers

Pulsed infrared laser energy was supplied by one of the two Lumonics TEA-620 CO₂ lasers available, which share the same resonator cavity. An attractive feature of these TEA-620 lasers is their ability to deliver a very short ($\sim 1 \mu\text{s}$), high energy pulse, up to 500 J each, while operating in the stable resonator mode with peak powers of 2.2 GW, according to the manufacturer. In the unstable resonator mode used throughout this work, the TEA-620 has a small output beam divergence measured in the sub-milliradian range, with pulses up to 300 J. Concerns about the limited lifespan of the high voltage capacitors and the potential damaging effects of supply-side over-voltage oscillations led to conservative decision to operate the 620s at 65 to 70 % of their rated maximum capacitor charge of 100 kV. This decision reduced the 620’s available output laser energy to a range of 150 to 230 J/pulse, but greatly increased reliability.

In future experiments these lasers will be configured to fire sequentially for multi-pulse LP experiments to examine the interaction of two laser-induced blast waves within a Lightcraft's absorption chamber, under simulated ultra-high PRF conditions (e.g., 10 to 20 kHz); throughout the present campaign technical issues forced operation at only single pulse mode.

These Lumonics TEA-620 lasers can operate with several different gas mixtures that produce different laser output pulse profiles and energies. The lasers currently operate in a “flow-through,” open-cycle mode wherein the gas mixture is controlled by varying the flow rate of each gas constituent. In the present test campaign a high gain (HG) mixture was used, which produced a short $\sim 1 \mu\text{s}$ pulse with a higher fraction of the pulse energy contained in the initial $\sim 90 \text{ ns}$ spike than in the long tail. The laser pulse characteristics achieved with this HG mixture are displayed in Table 1.

Table 1 Lumonics TEA-620 laser pulse characteristics with high gain gas mixture.

<i>Parameter (units)</i>	<i>Value</i>
Energy per pulse, J	150-230
Wavelength, μm	10.6
Peak pulse duration (FWHM), ns	90-100
Maximum peak power, MW	~ 1800
Total pulse duration, μs	~ 1.0
HG gas mixture flow, ft^3/hr	16.0 He; 6.5 CO_2 ; 3.2 N_2
Power supply voltage, kV	65-70

During the TEA-620's refurbishment process, a new set of optics had to be designed and an *unstable* resonator (cavity) was selected over a *stable* resonator configuration. This was considered necessary due to the long beam path from laser to HST test section ($\sim 25 \text{ m}$), since the unstable resonator results in a beam with reduced divergence, even though the output pulse energies are considerably lower (e.g., 320 J vs. 500 J from each 620 module).

For the laser transmission to the HST, a special “light-tight” laser beam delivery path was assembled, starting at the 622 laser, encountering a sequence of optical elements (i.e., the “optical train”) which are arranged in the order shown in Fig. 3: First, the beam leaves the laser output coupler with a diameter of 254 mm (10 in) and arrives at the 0.75x magnification (reducing) telescope, after reflecting off the concave mirror, the incident beam strikes a 228.6 mm (9 in) diameter convex aluminum mirror placed 1.25 m away, requiring a mirror curvature of 7.5 m to regain beam collimation. This reduced aperture beam fit nicely through the three 300 mm diameter turning mirrors and clears the 200 mm aperture window installed with a 7 deg. incidence at the HST hollow sting depicted in Fig. 2. This 250 mm diameter, 50 mm thick NaCl window serves a dual purpose: 1) a physical boundary to isolate the high vacuum dump tank volume (necessary for the HST

operation) from the lab environment; and, 2) a beam splitter that diverts a small portion of laser pulse energy to a beam diagnosis optical table.

Approximately 8% of the incident $10.6\ \mu\text{m}$ beam energy is diverted to the optical table, onto a concave copper mirror of 250 mm diameter and 2 m surface radius, which concentrates the focused beam through a second NaCl window and onto a Gentec UP60N-40S-H9 thermopile calorimeter. This second oblique NaCl window diverts $\sim 0.64\%$ of the laser energy into a Hamamatsu B749 photon drag detector, for the measurement of the pulse profile¹.

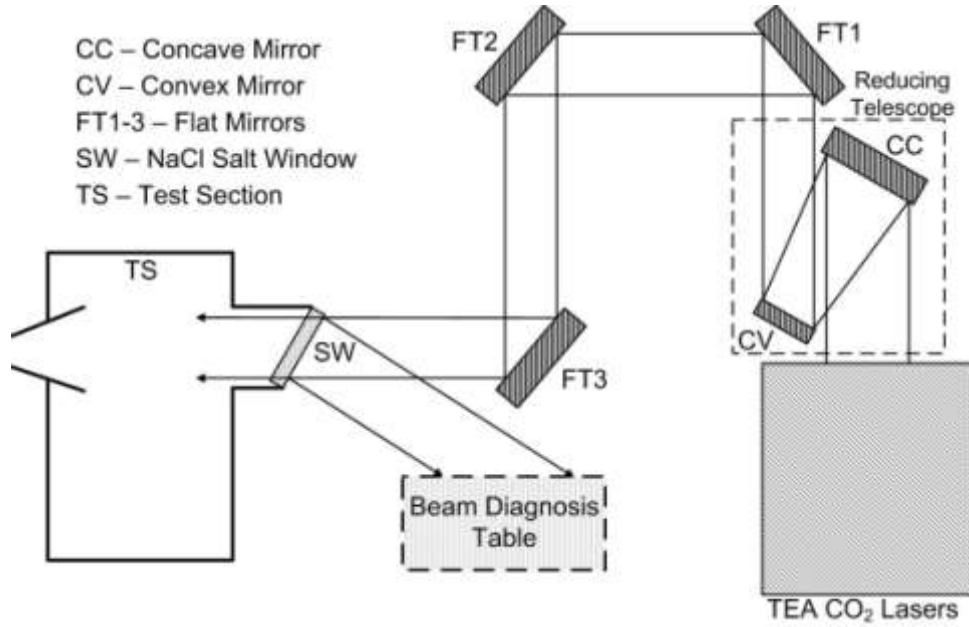


Fig. 3 Laser beam transmission path through the laboratory to the test section.

This beam diagnostics table was set up for measuring laser pulse energy for every test run, with the setup being calibrated with the use of two calorimeters: 1) one placed inside the HST test section, just downstream of the 2D Lightcraft model (Sciencetech Astral Series S, 200 mm aperture) to capture the actual energy incident onto the test model, and, 2) a second calorimeter placed outside, near the sting, to collect the reflected portion of the beam (Gentec UP60N-40S-H9) entering the sting window. The beam-splitter calibration plot is given in Fig. 4, together with the linear fit results and corresponding instrument measurement error. The laser pulse profile was obtained with the use of a secondary beam-splitter and a photon drag detector, and is dictated by the laser kinetics for the gas composition filling the active cavity volume. It is also dependent on the final Marx bank voltage, available energy, and discharge dynamics. The energy profiles sampled throughout this experimental campaign revealed little variation, since the laser gas mixture composition was kept unchanged. The pulse profile in Fig. 5 indicates that approximately 70% of the pulse energy resides in the spike, with the remaining 30% in the $1.5\ \mu\text{s}$ pulse tail.

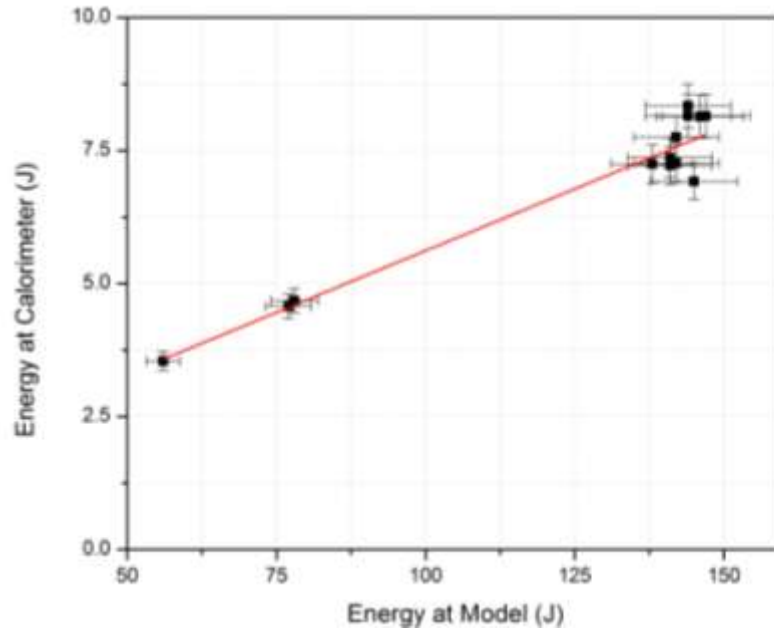


Fig. 4 Beam-splitter energy calibration curve for NaCl sting-window.

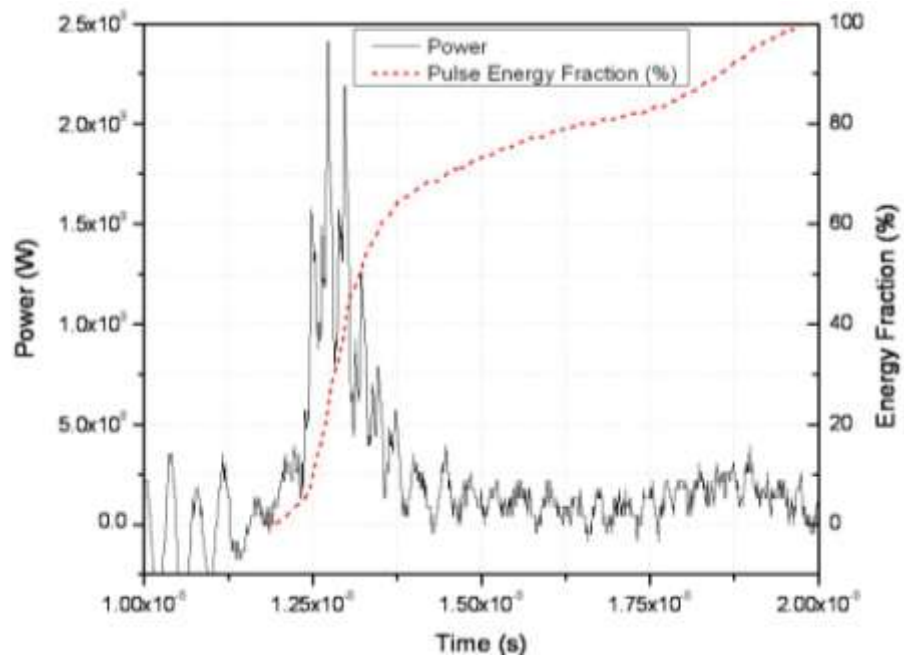


Fig. 5 Laser pulse profile and integrated pulse energy sampled at NaCl sting-window.

C. 2-D Cross Section Lightcraft Model

This 2-D airbreathing engine model is approximately a half-scale representation of a 1/24th annular section of the 1.4 m diameter LightCraft Technology Demonstrator (LTD) analyzed^{2, 6} by the now-defunct SDIO Laser Propulsion Program, and is scaled to fit inside the HST 0.6 m T3 test section. A derivative of previous LP research performed at RPI, the 250 mm wide, 2-D aluminum model is comprised of three basic parts: i) forebody compression ramp; ii) inlet/shroud; and, iii) primary parabolic mirror/expansion surface. The external compression inlet forebody directs the captured airflow, across the shroud's flat plate (lower) impulse surface that bounds the laser absorption chamber. When the incoming laser beam is brought to a line focus (as shown in Fig. 6) upon this shroud undersurface, the aluminum "igniter" material greatly lowers the incident laser intensity and fluence required to trigger the optical air breakdown⁷.

The geometry for this model's external compression air inlet is similar to that studied in the past, but the length was truncated to represent only part of an actual scale nosecone in order to fit within the T3 HST nozzle. Fig.6 depicts the 2-D model contour together with the position of the pressure sensors. The compression ramp section is instrumented with 3 pressure transducers (P_2 , P_3 , and P_4) distributed lengthwise along the centerline.

Following the compression ramp, comes a smooth transition or "throat" section just upstream of the primary focusing optics. This rear parabolic reflector has three main functions: 1) focus the incoming laser beam to cause the electrical air breakdown on the shroud undersurface; 2) act as an inner lower boundary of the absorption chamber, containing the subsequent cylindrical blast wave generated by laser induced breakdown; and, 3) participate as an expansion surface for the blast-wave-processed engine in the case of a working airflow. In this 2-D model the primary reflector is composed of a sturdy aluminum "hardback" machined with the desired parabolic contour, to which a polished OFHC copper faceplate was attached to create the 2-D mirror; this optic geometry was sketched for unrealized LP proposed experiments. The primary rear reflector was fitted with four pressure sensors (P_{10} thru P_{13} in Fig. 6).

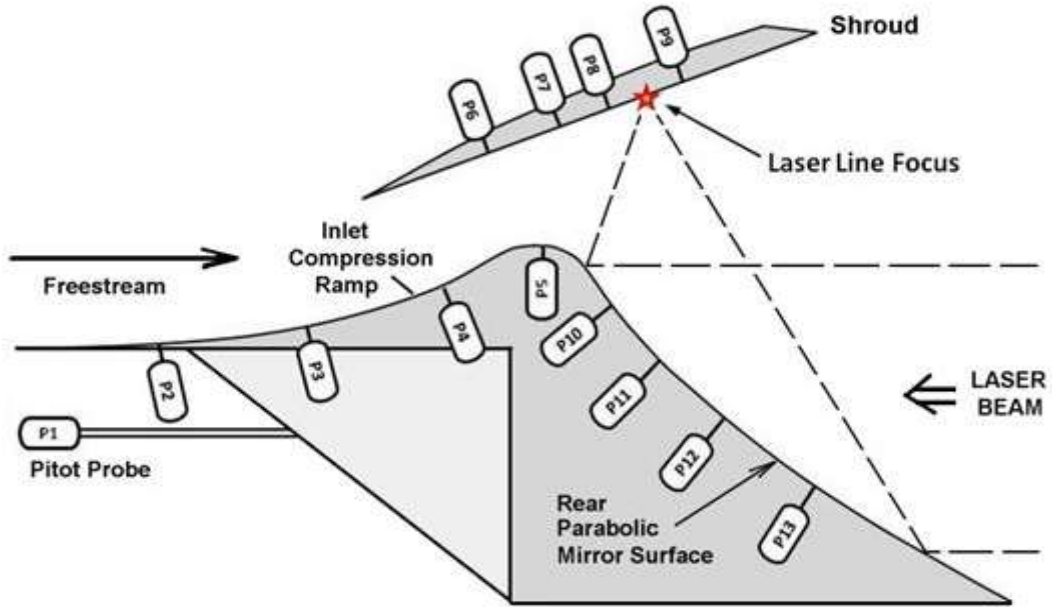


Fig. 6 Pressure sensor positions within 2-D model geometry.

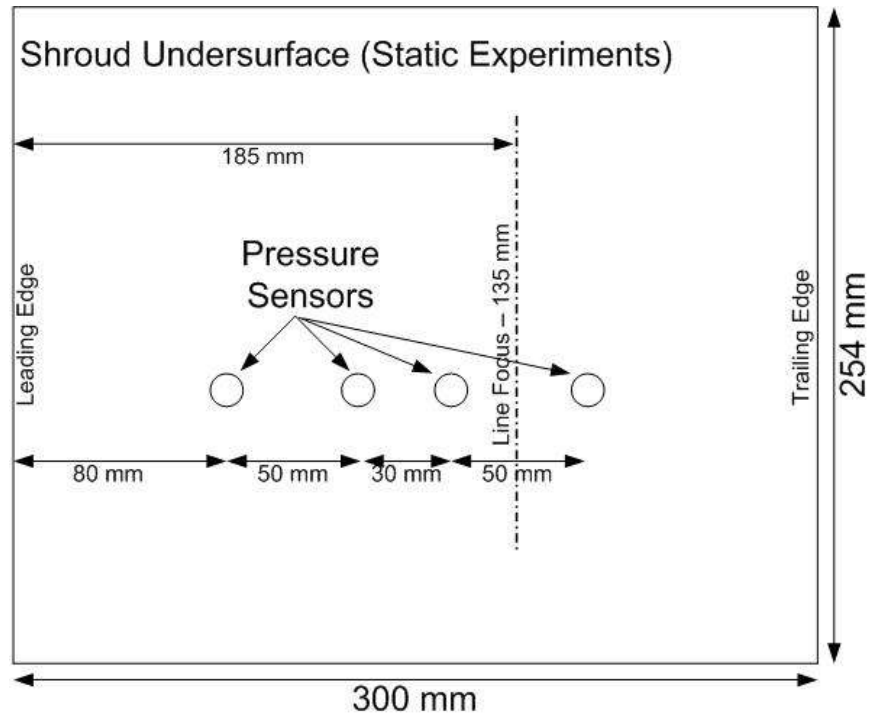


Fig. 7 Sensor disposition on shroud undersurface and line focus position used during the static experiments.

The 2-D shroud provides both air inlet capture and absorption chamber functions and it is comprised of a simple planar inner wall, with a streamlined cylindrical exterior surface that is of lesser importance in the current experiments; the shroud

was also fitted with four pressure transducers (P_6 thru P_9 in Fig. 7). Figure 8 shows the model installed in the HST test section.

Because of the varied test conditions that can be simulated in the HST, the 2-D laser ‘scramjet’ model was designed in a modular manner so that most parts can be exchanged with the current configuration—considered the first in a series of Lightcraft engines to be tested in the near future. The shroud can be placed at different positions with respect to the model’s center-body (i.e., compression ramp + primary reflector), since the mechanical support system for the articulating shroud was designed for three degrees of freedom: 1) fore and aft translation; 2) up and down translation; and, 3) free rotation for changing angle-of-attack. For the static (i.e., quiescent flow) experiments performed in this work, the laser line focus was kept at the same axial position upon the shroud undersurface as shown in Fig. 7; to change angle-of-attack for the experiments, the shroud is simply rotated about this line focus. During these hypersonic experiments, the axial focal line position was varied across the shroud to accommodate desired test conditions.

The influence of the radially expanding flow field exiting the HST conical nozzle was neglected in the present experiments; the hypersonic flow is “channelized” to some extent by the 2-D model’s polycarbonate side panels. The principal function of the side panels was to support the shroud while providing an unobstructed view of the laser-induced gasdynamic phenomena taking place within the absorption chamber. These side panels introduce oblique shock waves into the engine interior flow field, phenomena which was deliberately not visualized (i.e., purposefully avoided) in the schlieren setup. Future detailed investigations of such shock-induced perturbations, as well as more detailed analyses of the external compression inlet characteristics, must await further instrumentation and testing. Nevertheless, to accomplish the principal research objectives of the present campaign (i.e., first-order analysis of impulse generation physics, and overall process efficiency), these perturbation effects can be neglected.

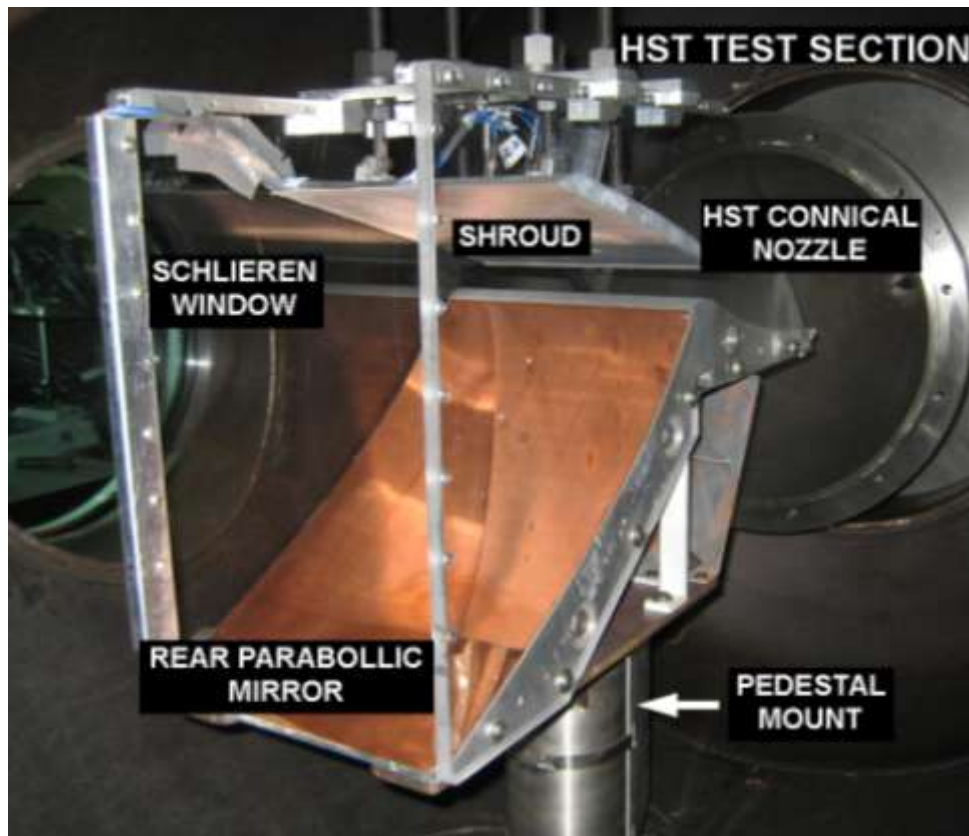


Fig. 8 2-D laser propulsion model installed in T3 hypersonic shock tunnel.

D. Instrumentation and Data Acquisition

A full diagnostic array is required to monitor all essential components of the experimental setup which includes the T3 HST (vacuum chamber), 622 laser system, and experimental model. The pressure inside the evacuated dump tank and test section of the HST is measured by a BOC Edwards APG-L-NW16 Active Pirani vacuum gauge, read by a Model 1575 pressure display.

The TEA-620 laser system is fitted with a Teledyne Model 3190 trace oxygen analyzer for measuring O_2 contamination levels in the laser gas mix, to assure that a “glow discharge” is established across the resonator electrodes instead of damaging arcs. Both TEA-620 lasers are controlled by a single customized control panel, with separate controls for the 100 kV Hypotronics power supply that charges the Marx capacitor banks.

The 2-D model was instrumented with thirteen piezoelectric PCB pressure transducers: twelve for measuring the pressure distribution vs. time along the model centerline, and one installed in a separate Pitot probe, used in later experiments for sensing the stagnation impact pressure of incoming hypersonic flow. Due to the high blast wave convecting speed, only the shroud pressure transducers were able to measure the blast-induced pressure increase, therefore all the resulting data analysis focus only on these sensors (Fig. 7).

An ultra-high speed Cordin digital camera was implemented with schlieren optical visualization setup for analyzing the time-dependent flow-field structure inside the 2-D absorption chamber; the objective was to capture the evolving LSD wave driven, expanding blast wave dynamics, and subsequent blast/flow interactions within the engine working fluid.

The mirror-based schlieren setup adopted a standard ‘Z’ configuration with two flat folding mirrors with the test section in between. A schematic of this system is depicted in Fig. 9. The effective viewing aperture 250 mm in diameter, dictated by the size of the quartz windows installed in the two test section ports bounding the test section. This schlieren system is composed of a pulsed xenon flash lamp, an optical slit and focusing lens, two parabolic and three flat mirrors, the knife edge which provides the necessary light cut-off, and the Cordin 550 rotating mirror, ultra-high speed camera.

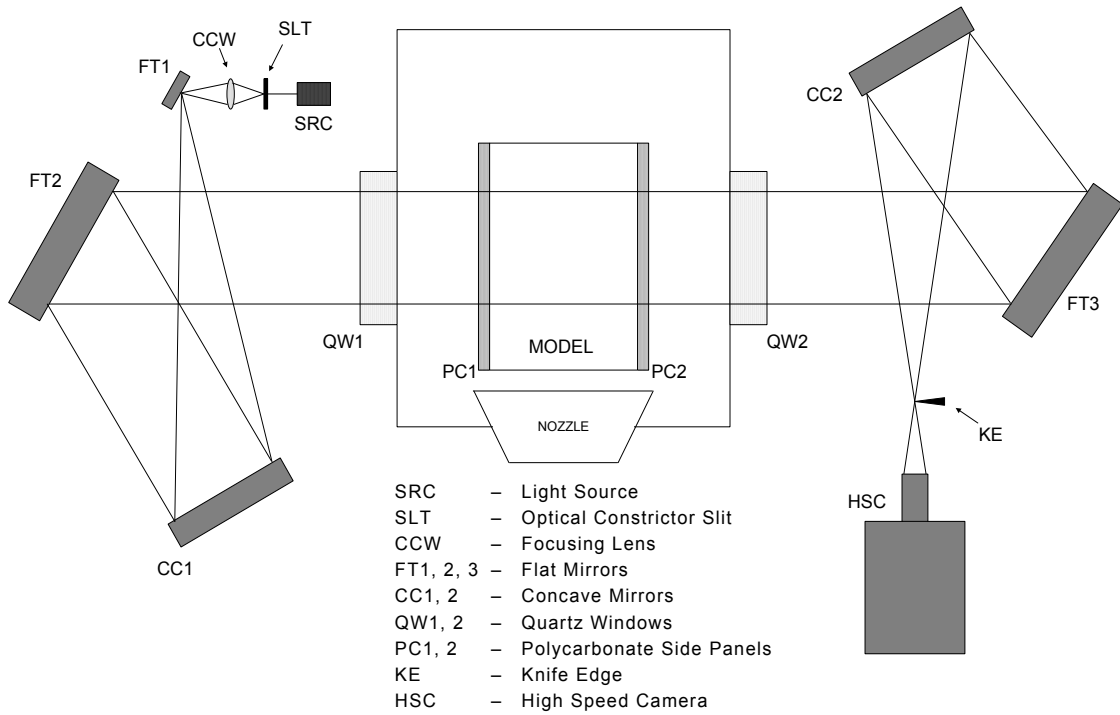


Fig. 9 Schlieren flow visualization system and Cordin camera system setup for T3 test section.

The Cordin 550 camera can acquire 32 frames with a maximum resolution of 1000 x 1000 pixels at up to 2 million frames per second (fps) in full color. Such frame rates are achieved by a multi-faceted mirror spinning at high speeds, surrounded by 32 CCD elements which acquire images as the mirror rotates. Mirror rotation is driven by a turbine wheel

supplied with high pressure N_2 for frame rates up to 500,000 fps, and pressurized He for the highest speeds. Even though extremely high speeds can be achieved, the present work demanded more modest 50,000 to 100,000 fps because of technical reasons related to the high Electro-Magnetic Interference (EMI) generated when the 620-TEA lasers were fired.

The data acquisition system required more than 18-20 channels, depending on the test objectives. For the 2-D Lightcraft model alone, 13 channels were needed for the Piezo-electric pressure transducers, additional channels were needed for TEA-620 laser diagnostics and even more are needed for hypersonic experiments where the T3 HST is completely active.

Two 16-channel Yokogawa DL750 Scoperecorders comprised most of the data acquisition system: one for the LP model pressure distributions, and the other for HST instrumentation. These DL750s can record up to 10 MS/s for all 16 channels for the duration of the test window. Raw pressure data from the model's Piezoelectrics was pre-amplified by a 16-Channel PCB 481A02 signal conditioner. The Yokogawa DL750 easily interfaced with the favored data analysis software (Microcal Origin), without the need for preprocessing. Data acquisition for the TEA-620's diagnostic instrumentation was performed by a Tektronix TDS2014 (100 MHz, 1GS/s); the laser pulse profile was sensed by a Hamamatsu B749 Photon Drag detector. The Gentec's UP-60N calorimeter readout was acquired by a Pentium PC computer. All remaining data gathered during the LP experiments (laser gas constituent feed rates, etc) was hand recorded from direct readouts on standard analog gauges and other stand-alone instruments.

E. Methodology

T3 hypersonic experiments were performed on the 2-D model with the intent of assessing the feasibility of laser powered flight for purely airbreathing Lightcraft engines in the Mach 6-10 regime. This section presents a qualitative analysis of the laser-scrumjet impulse generation process and dominant features, identified from high-speed schlieren flow visualizations of the flow structure, along with measured pressure histories over inner surfaces of the 2-D engine's laser absorption chamber. Quantitative results and discussions are limited to cases/runs in which the desired experimental conditions were achieved.

The objective of these ground tests was to explore the hypersonic performance of a laser Lightcraft engine along an airbreathing flight trajectory to low Earth orbit. The hypersonic shock tunnel (HST) is known to be the flow facility of choice, in duplicating such environmental conditions. The two principal parameters that assure similitude are the Reynolds number and Mach number. Matching of these two nondimensional parameters is necessary to achieve similitude in velocity and pressure; however, if similitude in temperature, heat transfer, reaction rates, and continuity are also to be achieved

(which exceeds the scope of the present work), additional parameters including the Prandtl, Damköler, and Knudsen numbers (among others) must be considered.

As mentioned earlier, the Lightcraft Technology Demonstrator (LTD) concept vehicle was used for the reference point in designing the present 2-D laser-scamjet model. An optimized Earth-to-orbit launch trajectory (Fig. 10) for laser launch was developed using SORT flight dynamics software. This altitude vs. Mach number trajectory was subsequently applied in numerical simulations of flow fields over (and through) various Lightcraft engine/vehicle geometries, at speeds ranging from low subsonic up to Mach 5. The Reynolds numbers encountered along this optimized laser-launch trajectory are plotted vs. Mach number in Fig. 11, along with T3 experimental conditions for the present test campaign. However approximate these flow conditions are, improved matching of similarity parameters must await future experiments, and model designs specifically tailored for such requirements. The existing 2-D laser-scamjet model was tested under “off-design” (inlet and absorption chamber) conditions throughout the hypersonic campaign, with more exact scaling of physical parameters (representative of actual flights) being a secondary, iterative objective for a subsequent campaign.

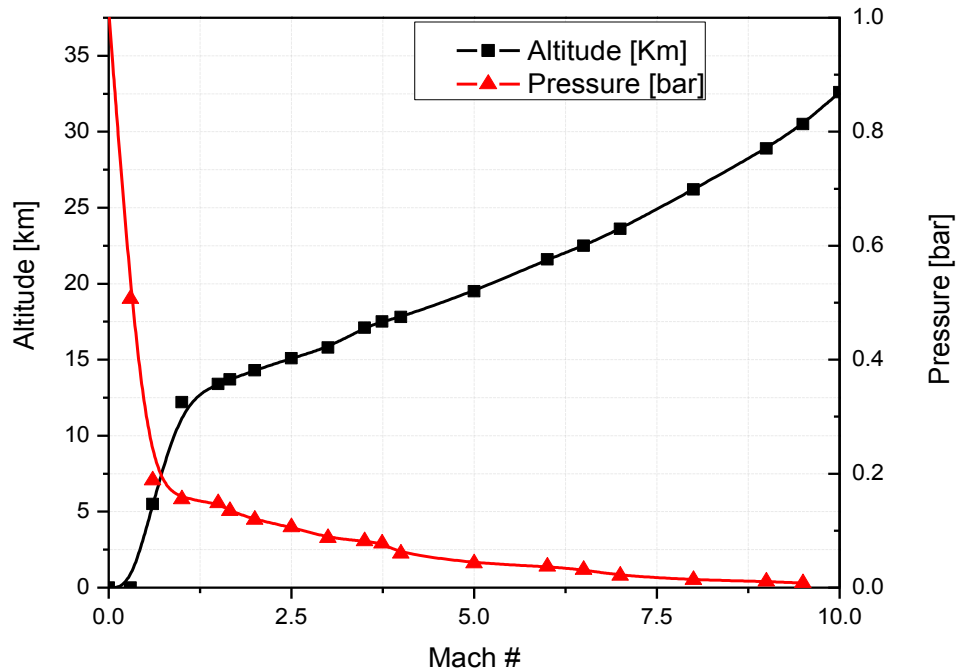


Fig. 10 Altitude vs. Mach number schedule for optimized airbreathing LP launch to low Earth orbit.

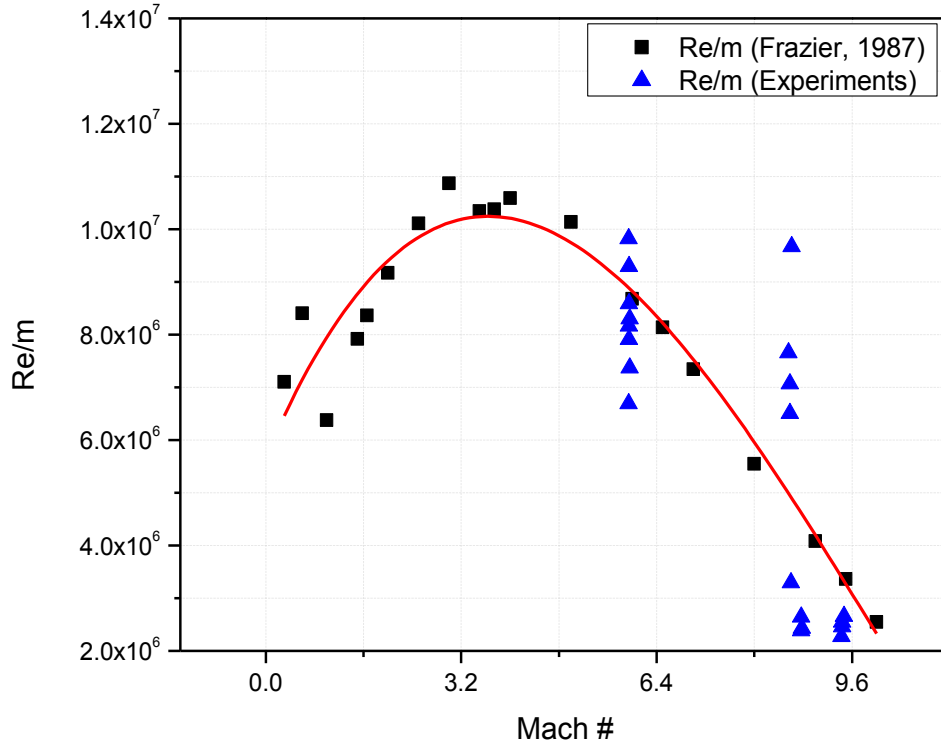


Fig. 11 Reynolds number variation with Mach number along optimized laser launch trajectory together with T3 HST data from present test campaign.

The direct measurement of the test section conditions in any ground test facility is possible only with the aid of proper sensors. Calculation of free-stream properties such as stagnation pressure and temperature is made from specific measurements from sensors positioned at critical locations throughout the tunnel. For the T3 HST facility, such instrumentation was described previously in the present report.

The STCALC code, developed at the HTN-LAH laboratory, was used to calculate free-stream properties incident upon the 2-D laser-scrumjet model, directly from gas conditions behind the incident/reflected shock wave at the downstream end of the driven section, which acts as the HST expansion nozzle's reservoir. This code accounts for real gas effects in the T3 tunnel, through the use of tabulated air properties assuming chemical and thermodynamic equilibrium. The code requires as input: a) the gas constant and specific heat ratio, b) the initial driven-section pressure and temperature, and c) the incident shock wave transit time through the driven tube. This transit time is measured by two pressure sensors located at known positions at the end of the driven section. The STCALC program requires the input of the measured reservoir pressure, instead of that calculated by reflected shock relations, which enables the calculation of both "*flow through*" operation, as well as for the operation in the "*reflected mode*" in the HST, wherein different reservoir conditions are achieved depending on the mode of operation. Several experimental conditions were selected for the current campaign (stagnation pressure,

temperature, and density, together with the incident and reflected shock wave Mach numbers), although some of these experiments results are not reported in this paper.

Once the reservoir conditions are obtained, the next step is the calculation of free stream flow conditions at the exit station of the conical nozzle, which is also the entrance to the test section. Two calculation modes can be used: one that assumes the nozzle area ratio, and the other takes pressure data from a Pitot probe positioned in the test section. For the results presented herein, the nozzle area ratio mode was used, for the entire campaign of 24 test runs, three different nozzle area ratios were used.

The T3 HST expansion nozzle is composed of three conical sections, for which the final section has an exit diameter of 610 mm. When the present hypersonic campaign began, the initial nozzle had an area ratio of 535.9 with a throat diameter of 26.3 mm—thus giving an isentropic expansion to $M=10$. Since the 2-D model had initially been intended to operate at Mach numbers up to 6, the final nozzle section was removed to reduce the nozzle exit diameter to 491 mm for an isentropic expansion of $M = 9.12$ (at the selected HST conditions). This also facilitated the installation of the 2-D model, by avoiding interference with the nozzle. Shortly thereafter, a new family of nozzle throat inserts and a new nozzle transition section were designed for the T3 HST, which now enable test section Mach numbers of 6, 7, 8, 10, 12, and 15—assuming isentropic expansion. Of these, only the $M=10$ insert was available at the start of the present hypersonic testing campaign, with future experiments to explore wider free-stream conditions.

Successful operation of the combined system—T3 HST, 620-TEA laser, high speed camera, 2-D model and HST diagnostics—required precise timing of all involved systems, exacerbated by the inherent complexity of the entire setup, and multiple short duration phenomena. The entire test-time-window supplied by the HST flow is on order of ~ 3 ms, whereas the TEA 620 spike (FWHM) lasts approximately 100 ns followed by a ~ 1 μ s tail; the laser induced air-breakdown, subsequent blast wave expansion, and downstream convection lasts no longer than 150 μ s. All these events must be triggered in the desired sequence with high precision and low jitter. Timing complexity is further increased by the need for acquiring diagnostics from HST instrumentation, TEA 620 laser, and the 2-D model's pressure transducers, beam diagnosis (energy meter and photon drag), and high-speed camera system. To assure proper timing for the experiments reported here, the delays were evolved from instrumentation signals acquired in prior runs, and the principal reference time used was the incident shock arrival time at the nozzle entrance. To assure that the flow over the model was fully established, the main trigger signal followed 1.320 ms later, which then triggered the data acquisition system, schlieren light source, and secondary trigger. This secondary trigger activated the laser with a 50 μ s delay and the camera with a 250 μ s delay. The camera pre-trigger was set at -220 μ s, so it actually started acquiring images before the laser fired.

Figure 12 displays HST instrumentation signals from four pressure transducers during a sample hypersonic run, whereby the pressure increase confirms passage of an incident shock wave. Shown are the measured reservoir and test-section Pitot pressure signals as well as incident shock transit (M_{i1} and M_{i2}) captured at ports 40 cm apart, upstream from the nozzle entrance. This figure provides insight to the time scales involved in sequencing the whole system, wherein the raise in the reservoir pressure is used as the reference for all trigger delays, as mentioned before.

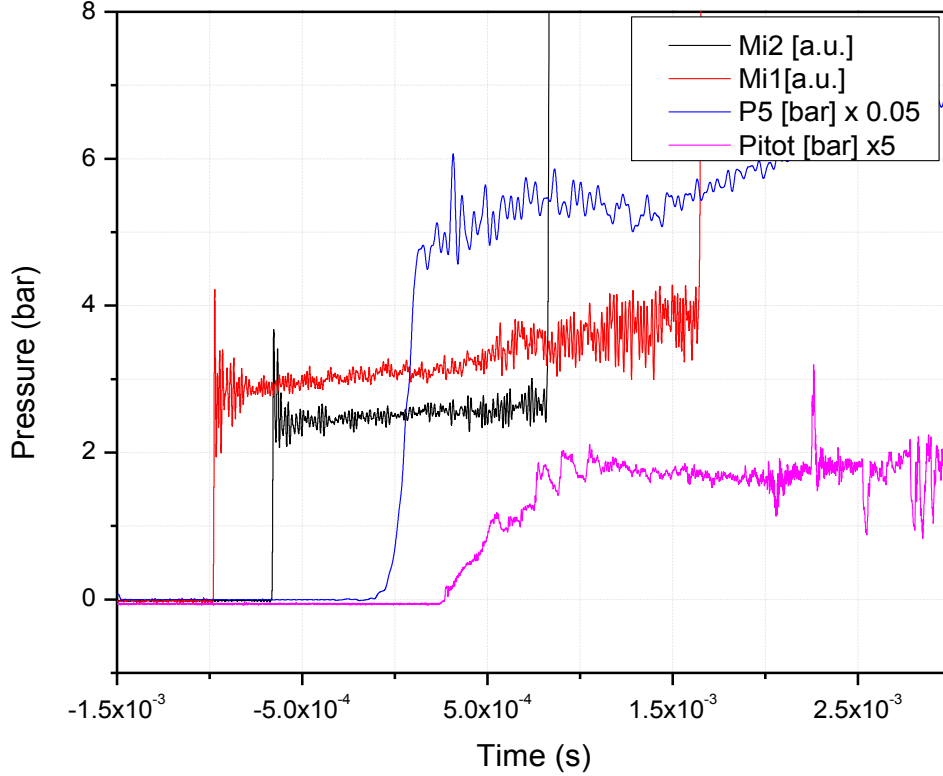


Fig. 12 Run#24 – Typical HST and Pitot pressure signals obtained during experiments.

Test-to-test variations throughout the hypersonic campaign were not restricted just to variations in HST test-section flow conditions. The entire 2-D Lightcraft model itself was tilted downward up to 10-degrees in some tests, and the shroud placement was frequently altered. The shroud support structure, as explained earlier, permits three degrees of freedom in movement; hence the shroud can be easily repositioned between runs to examine flow structures over the new geometries.

The entire model was tilted downward at 0, 4, and 7.5 degrees from horizontal, providing stronger inlet bow shock waves, larger inlet capture areas, and more highly compressed inlet flows. This was explored to help ameliorate the ‘off-design’ inlet operation (i.e., without the triangular flat plate forebody extension). Note that the LTD engine/vehicle geometry was designed for lower design Mach numbers of 5 and below, and much higher laser pulse energies (e.g., linear energy density at the focal line up to 87.5 J/cm around the 1.2 m diameter focal ring).

F. Hypersonic Campaign Results

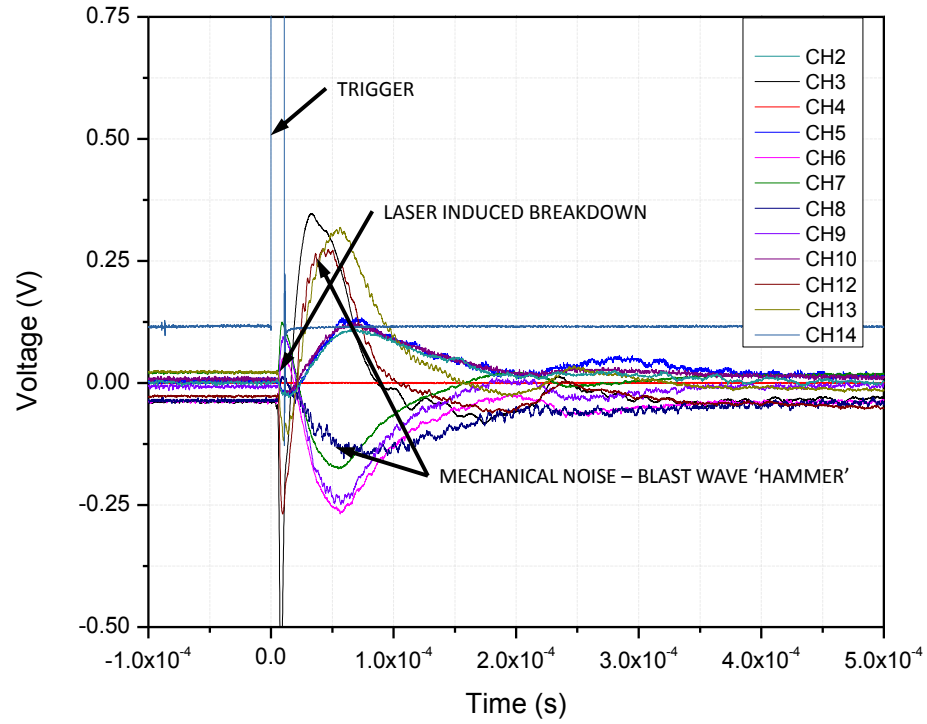
This section provides an analysis and discussion of the 24 runs with the 2-D laser-scrumjet model that comprise the hypersonic test campaign. These results are grouped by similar test section conditions (free-stream properties and Mach number), and model configuration—specifically: a) center body inclination with respect to HST nozzle axis, and b) shroud leading edge (L.E.) distance from the laser focal line, and shroud pitch with respect to the nozzle axis.

The initial runs were carried out at $M \sim 8.6$ with the shroud was set at -25° inclination. The driven section was pressurized to 2.5 times atmospheric with synthetic air. During these first runs three different situations were analyzed: 1) Laser ON with hypersonic flow; 2) Laser OFF with the same hypersonic flow conditions; and, 3) Laser ON while the model was rested in the evacuated dump tank right before the onset of the test flow.

From the pressure data obtained over the model during these runs, it could be seen a simultaneous response of the signals at every sensor when the laser was fired. This does not correspond to the pressure increase from the laser-induced blast, which has to take place with a delay between sensors, as the blast wave expands, and shown in the previous chapter at static conditions.

This behavior was found to be caused by a ‘hammering effect’ produced by the laser induced breakdown and subsequent blast over the surface of the shroud with reduced local pressure, analog to a hammer impact at the laser focal point. This response is not seen at higher ambient pressures due to a larger amount of the laser energy being transferred to the air at the inner surface of the shroud. This mechanism of energy transfer to the shroud surface behaves as a ‘soft hammer’, dampening the mechanical impact caused during the process. This differs from the case of a near vacuum environment where little of the breakdown energy is absorbed by the surrounding air.

The complete mitigation of this ‘hammer’ effect is a difficult task however; reduction of its influence on the pressure data can be achieved with a different design for the shroud fixation and use of a sturdier model less prone to the effects of vibration. This is performed by the use of strain isolated pressure transducers as well as ‘check’ transducers. This enables for the documentation of the vibration response alone, guiding modifications to the model until their output becomes negligible. Furthermore, pressure port inserts can be manufactured with low density material providing a higher level of mechanical insulation for the sensor.



RUN#1-All

Fig. 13 Run #1-Pressure transducer traces for Ch2-14 (distributed over 2-D model); Laser ON, Flow ON; $M=8.61$; $E_p=196\pm20$ J. Channel number corresponds to pressure sensor. Note simultaneous sensor response to laser-induced blast, indicating excessive mechanical noise.

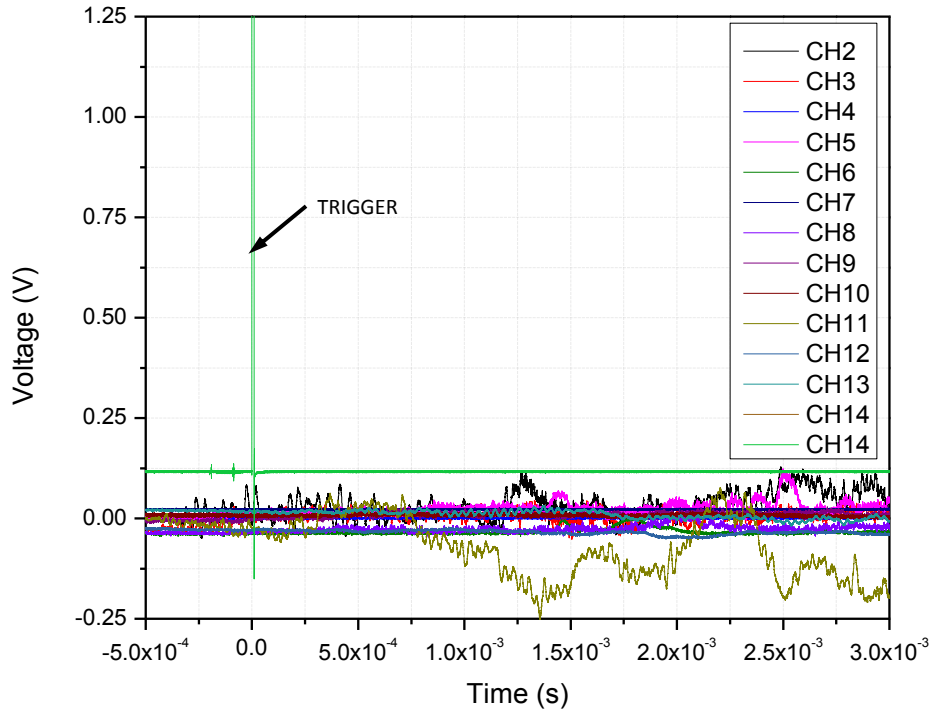
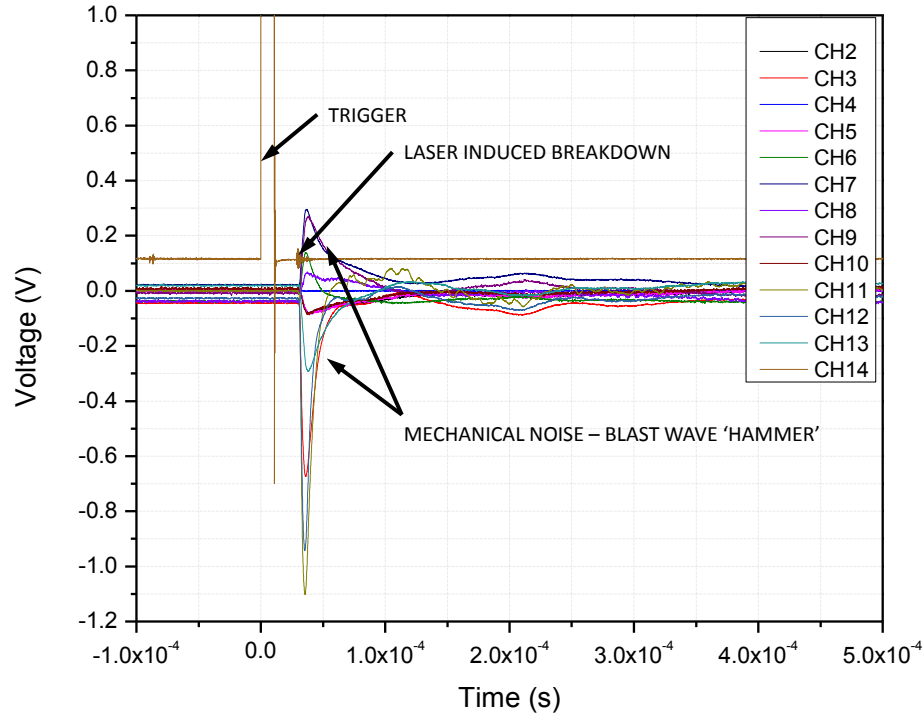


Fig. 14 Run #2- Pressure transducer traces for Ch2-14 (sensors distributed over 2-D model); Laser OFF, flow ON; $M=8.56$; $E_p=0$ J. The signal stability throughout the time window indicates fully established hypersonic flow over the model.



RUN#0-All

Fig. 15 Run #0-Pressure transducer traces for Ch2-14 (sensors distributed over 2-D model); Laser ON, flow OFF; $M=7.8$; $E_p=180\pm20$ J; $P_\infty=7.5E-02$ mbar. Note similarity to Run#1 results, in Fig. 13.

During this phase the high speed camera used for the schlieren imaging of the phenomena operated erratically due to the EMI noise generated by the TEA 620 lasers. Most of the 32 frames available for the camera acquisition were lost, with some of the visible frames left in a scrambled order. Only the runs performed without laser energy deposition were flawlessly acquired.

EMI problems with the high speed Cordin camera were eventually resolved (with a specific pre-trigger) during the next phase of troubleshooting experiments, along with other issues affecting the experimental setup. The complete solution of the EMI problem would entail an experimental setup with the laser completely shielded (isolate) from the camera system, to avoid the 2.0+ GW pulse (Marx capacitor bank) from interfering with the high-speed camera CMOS logic (+ 3V).

During Run #10, the laser was active and the pressure distribution over the model was acquired. This run was performed at $M=8.7$, with the model shroud inclined at -34 degrees, in an attempt to capture the shock wave generated off the compression ramp; the shroud axial position and the 'focus-on-shroud' restriction were maintained. The results obtained are in accordance to those from the previous experiments, with the mechanical noise making impossible the accurate measurement of the pressure increase caused by the laser induced blast wave expansion. This situation was emphasized by the extremely small capture and inlet area, aided by the reduce flow pressure and density at the focus.

At these conditions no blast wave expansion visualization was possible by the schlieren technique, with only the air-breakdown glow being distinguishable, as shown in Fig. 15. The acquired signal from the under-shroud pressure sensors (P6, P7 and P9) are displayed in Fig. 16, where the initial simultaneous peak can be clearly seen. The P8 presented problems and its signal was lost, and prompt replacement of the sensor was considered but had to be discarded due to technical issues concerning access to the sensor and cabling installation. Figure 16 clearly show the result of the blast wave ‘hammer’ effect and the subsequent increase in noise caused by the arrival of the expanding blast. Due to its proximity to the focus, sensor P9 shows a distinguishable peak from the pressure increase caused by the incoming blast, which was not present in P6 and P7, due to their distance from the focus, with the blast reaching them with greatly reduced strength.

Following the solution of the issues with the HST, the efforts were concentrated on the TEA 620 lasers, which were experiencing power supply premature discharge. These problems were solved with a major overhaul and enabled the successful operation during the remaining experiments.

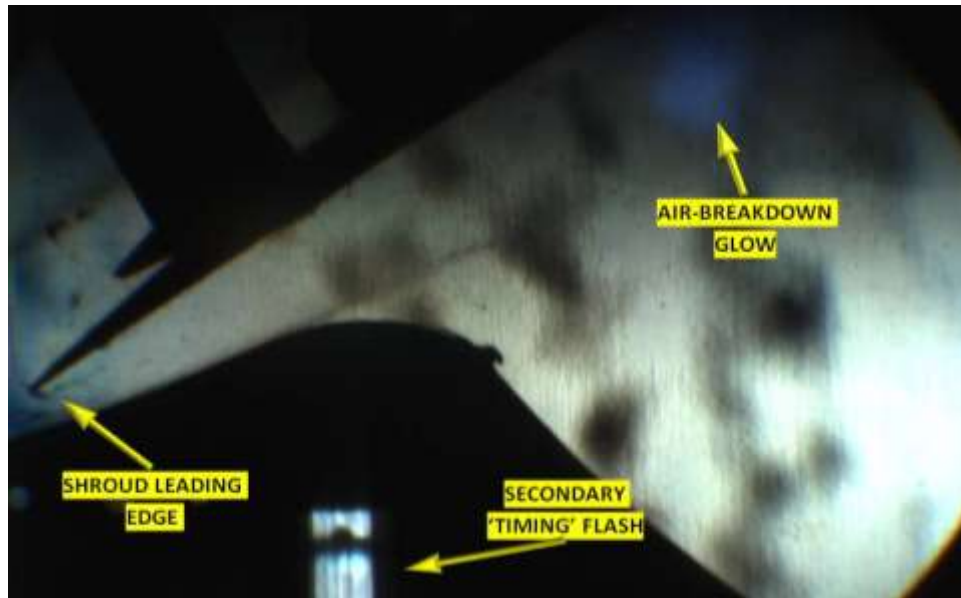


Fig. 15 Run#10 – Schlieren image with only the laser-induced air-breakdown glow visible. ($M=8.77$, $T_\infty=68.7$ K, $P_\infty=0.15$ kPa).

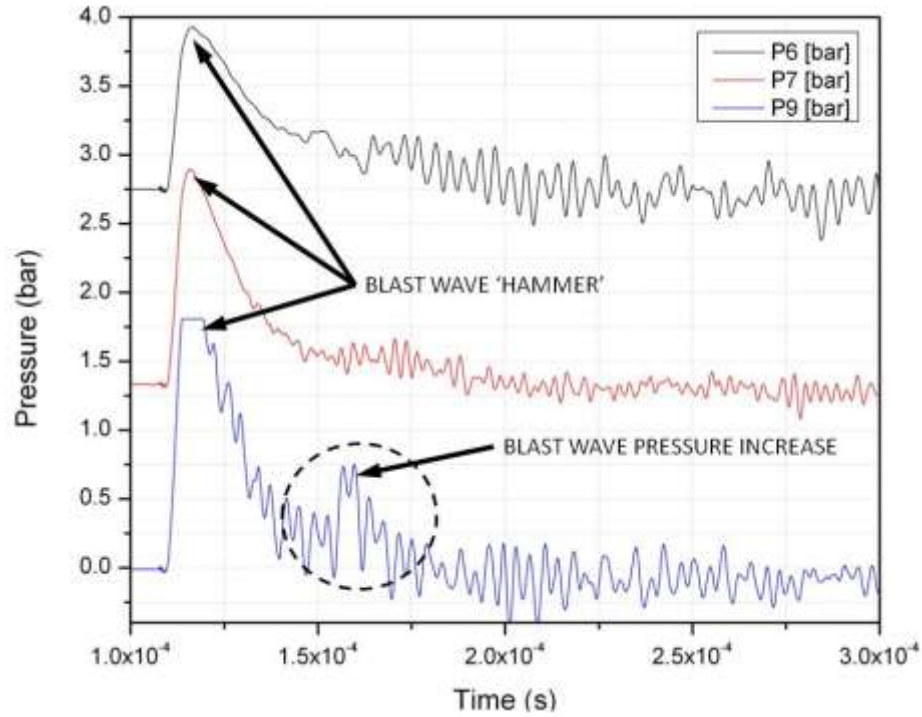


Fig. 16 Run#10 – Pressure gage traces for P6, P7,P9 distributed over shroud under-surface; laser ON, flow ON; Mach 8.77; $E_p=207J$. Sensor P9 pressure jump is from passage of blast wave.

Previous attempts to capture high-speed schlieren movies of laser-induced blast waves within the laser ‘scramjet’ engine were unsuccessful for two main reasons: 1) The low static pressure at the laser focal line, caused by the rapid expansion (and acceleration) of flow captured through the inlet gap, lead to weak laser-induced air breakdowns and blast waves; and, 2) the 620-TEA’s EMI pulse disrupted the Cordin camera, causing erratic behavior—i.e., frame scrambling, blank frames, and loss of trigger precision. Solutions to these two issues were discovered in this test series, finally enabling the acquisition of desired data.

The EMI solution emerged from a creative application of the camera’s pre-trigger and banks that record photographic frame sequences. The Cordin 550 is fitted with eight CCD camera banks that capture four frames each. Previous to receiving the trigger signal, these banks are continuously acquiring and storing images into the camera’s cache. With the proper pre-trigger, these banks are sequentially activated to deliver previously-acquired images that are stored in the cache memory. This pre-trigger procedure creatively circumvented the former EMI-induced camera disruptions.

For Run#16 ($M=5.96$; $T_\infty=258.3\text{ K}$; $P_\infty=5.32\text{ kPa}$; $E_p=187\pm19\text{ J}$), the shroud was set at -4° incidence (from horizontal), with the under-surface positioned slightly above the primary optics’ focal line. The entire model was pitched further forward from -7.5° (counterclockwise). A six-frame schlieren image montage from Run #16 is displayed in Fig. 17, wherein the shock wave off the lower leading edge of the shroud is clearly visible. The bow shock wave formed over the inlet

compression ramp/forebody meets with the shroud's shock wave at a point near where the laser-induced breakdown occurs. As it is convected downstream, the resultant expanding blast wave appears to interact with the shroud under-surface (see image at 22.6 μs); however, the reflected shock off the shroud under-surface appears unaffected. Also, note the secondary shock that has formed off the inlet compression ramp/forebody; it may be triggered off a small surface discontinuity on the inlet compression ramp just before the cylindrical transition section to the rear optics. Figure 18 gives the pressure traces measured by the PCB sensors across the shroud under-surface. The blast wave arrival times are clearly registered by P9 and P7, but negligible perturbation is seen by P6.

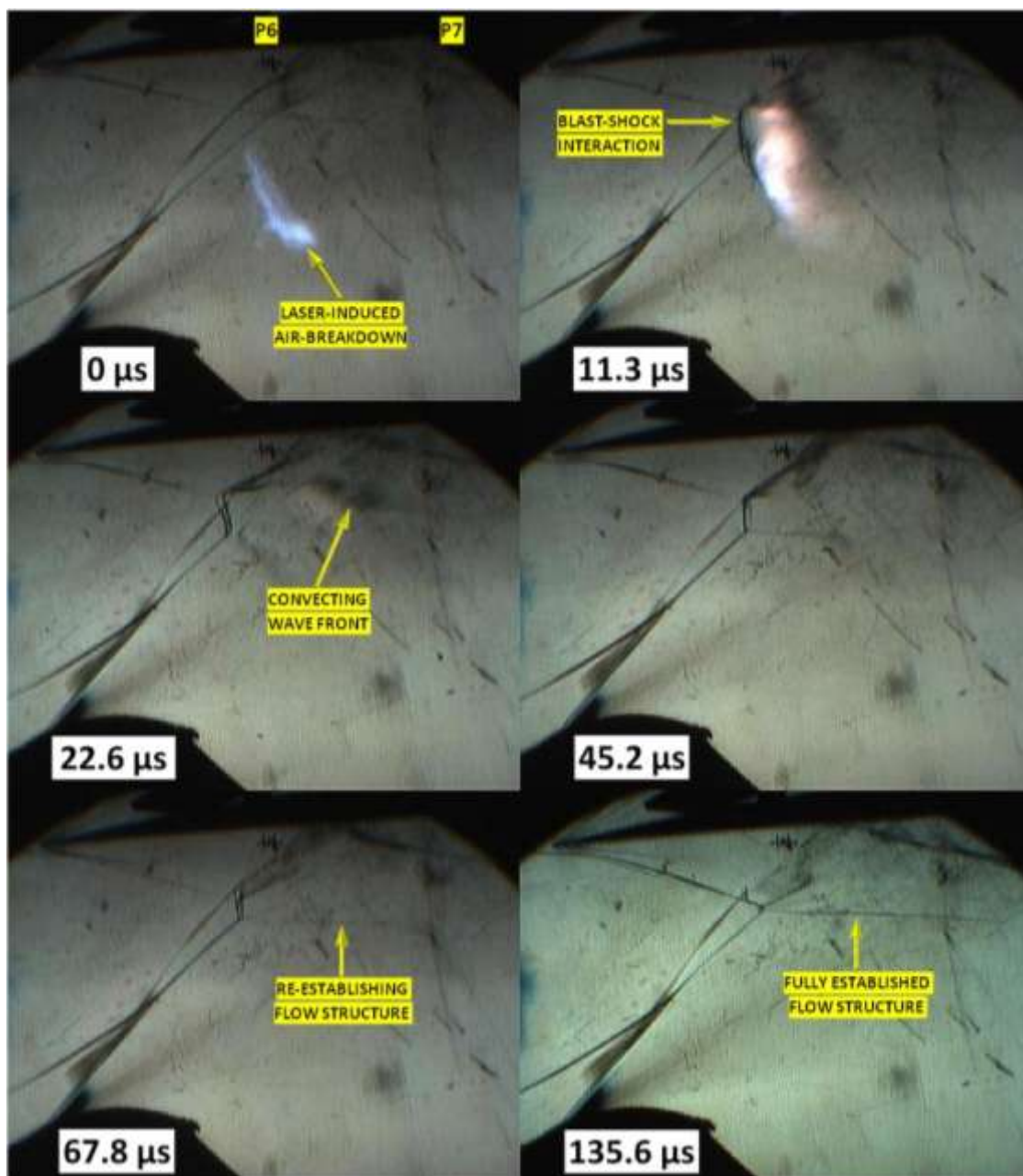


Fig. 17 Run#16 – Laser induced blast wave interaction with oblique shocks from shroud and inlet center-body at 7.5° inclination. ($M=5.96$; $T_\infty=258.3$ K; $P_\infty=5.32$ kPa; $E_p=187\pm 19$ J)

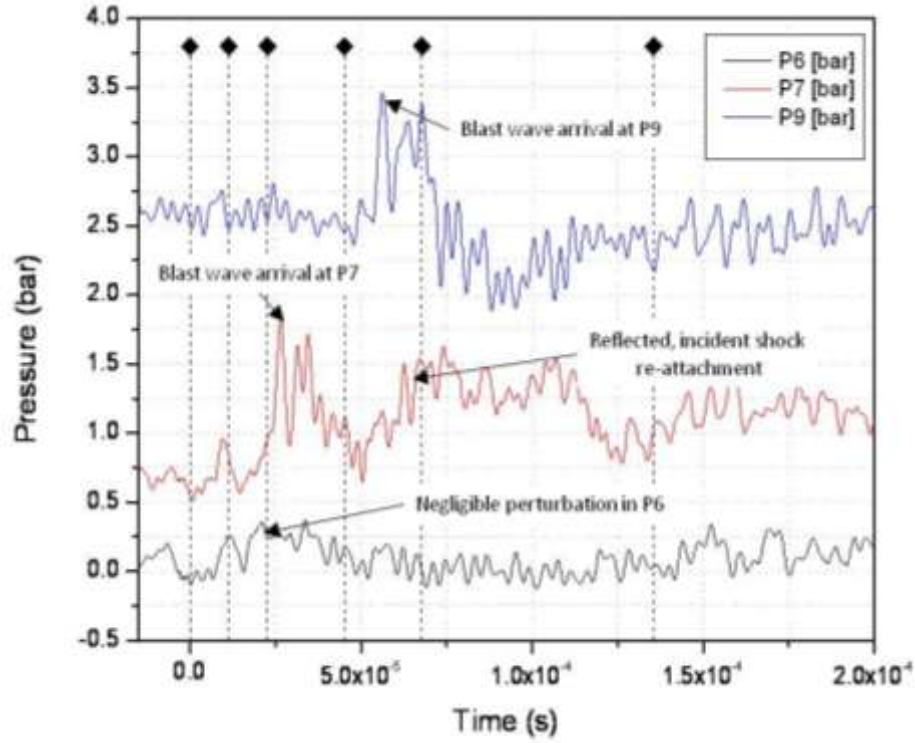


Fig. 18 Run#16 - Measured pressure distribution over shroud under-surface; traces offset. schlieren frames from Fig. 17 are marked by diamonds.

Run 17 was performed with the same HST setup configuration used in Run 16, but the schlieren images in Fig. 19 were considerably different, perhaps in large part because of dissimilar free-stream conditions ($M=5.94$, $T_\infty=256.8\text{ K}$, $P_\infty=6.25\text{ kPa}$, $E_p=186\pm19\text{ J}$) in the test section. The 19% increase in P_∞ and 22% increase in ρ_∞ between Runs 16 and 17, was likely caused by atypical rupture dynamics of DDS diaphragms. Considering the driver pressure of 3000 psi for Run 17, and 3250 psi for Run 16, the latter was expected to give higher free-stream P_∞ and ρ_∞ properties. A similar discrepancy was observed in Run 18 ($M=5.94$; $T_\infty=284.4\text{ K}$; $P_\infty=4.88\text{ kPa}$; $E_p=121\pm12\text{ J}$) in which the driver was charged to 3200 psi, but the test registered lower free-stream properties than either Run 16 or 17.

Despite the differences in test section free-stream properties, and diverse laser-induced blast-wave dynamics captured in the schlieren movies, Runs 16 and 17 displayed very similar pressure distributions across the shroud under-surface. A comparison of these distributions in Fig. 18 (Run 16) and Fig. 21 (Run 17) reveals that the blast wave in Run 16 propagated further upstream on the shroud before dissipating – note the small perturbation in the P6 signal; a similar response was not registered in Run 17, however. Other features observed in the Run 17 schlieren images (Fig. 19), and long exposure photograph in Fig. 20 are: 1) a more pronounced interaction of the laser-induced blast wave with the pre-established flow structure and shroud; 2) earlier re-stabilization of the disturbed flow field, probably accentuated by the higher free-stream P_∞ and ρ_∞ .

For Run 18, the shroud was pitched to -7.5° (further counter-clockwise), to align its under-surface parallel with the model center-body which was kept at -7.5° from horizontal; the free stream P_∞ and ρ_∞ were considerably reduced relative to the previous runs; and, the laser pulse energy of 121 ± 12 J was also lower. Several important features are captured in the Schlieren images of Fig. 22. Note the bifurcated shape of the laser-induced breakdown in the first image (also appearing in Fig. 19), and the subsequent sequence—possibly portraying the dynamics of an inlet “unstart”—which could be due to two factors: 1) the reduced static pressure under the shroud, thus less resistance to blast wave propagation upstream; and, 2) the lower shroud pitch angle (-7.5°) with respect to free-stream flow, causing a weaker shock off the shroud leading edge. These results are corroborated by the PCB traces in Fig. 23, which track the blast wave arrival at P6, P7, and P9, and subsequent re-establishment of the flow after the disturbance is swept downstream.

As seen in Figs. 17, 19, and 22, an oblique shock wave is attached at the shroud leading edge, despite the 7.5° negative inclination with respect to the test section axis. This result supports the hypothesis that the smaller (491 mm) HST nozzle exit delivers a conical expanding flow field into the test section with a non-negligible radial component striking the inclined 2-D model and shroud, which is a clear departure from the desired condition of quasi-parallel flow over the model in the test section. In the following Runs 21-23, this effect was reduced, albeit not entirely mitigated, with the reinstallation of the last section (610 mm) of the HST expansion nozzle. Future tests may have to employ reduced size Lightcraft engine models, to keep its boundaries within the central core section of the expanded flow field where the parallel flow assumption is valid.

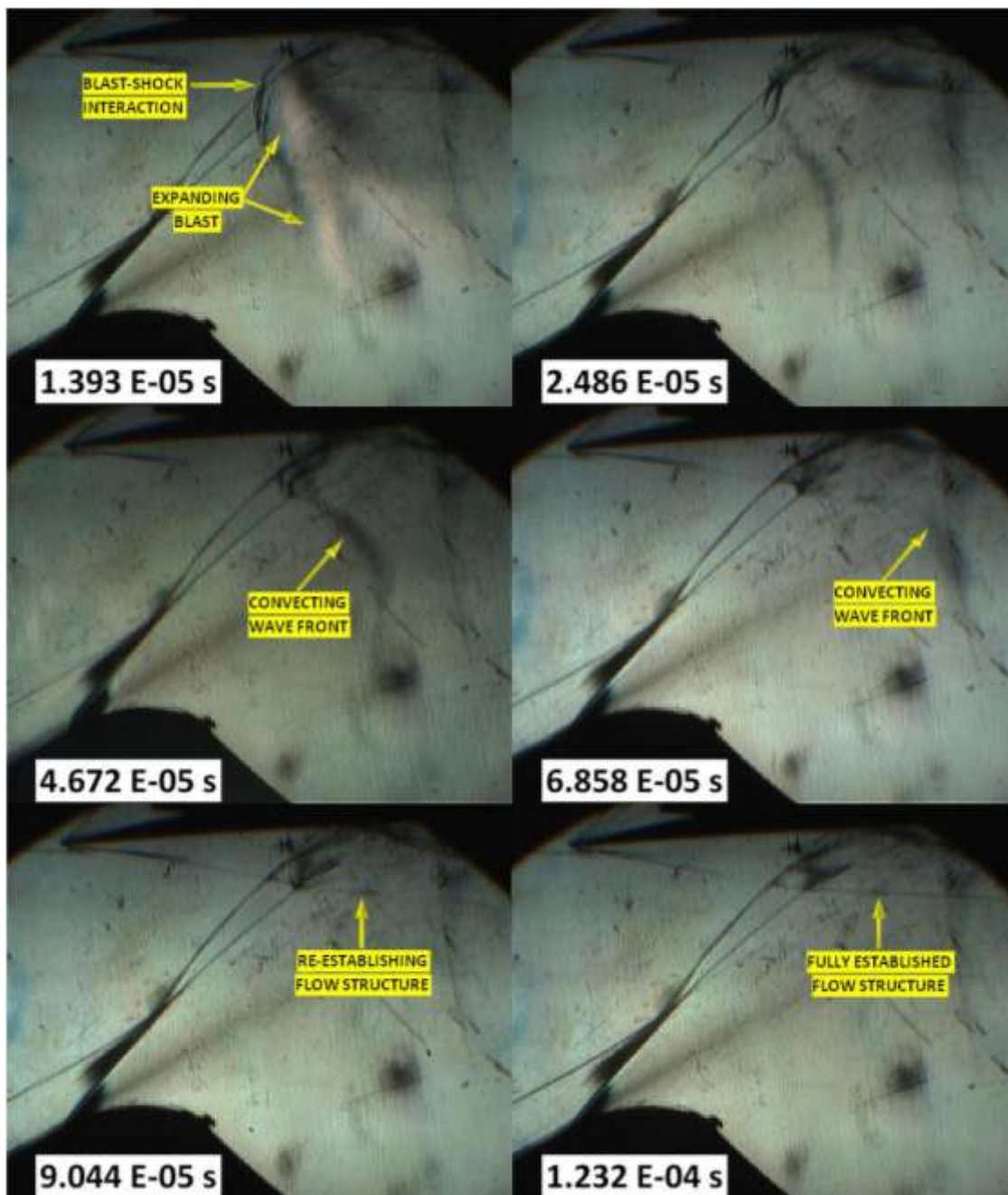


Fig. 19 Run#17 - Laser induced blast wave interaction with oblique shocks and shroud under-surface; 2-D model at -7.5° ; Shroud at -4° inclination. ($M=5.94$, $T_\infty=256.8$ K, $P_\infty=6.25$ kPa, $E_p=186\pm 19$ J)



Fig. 20 Run#17 - Long exposure color photograph of laser-induced breakdown geometry at Mach 5.96; 2-D model at -7.5° ; Shroud at -4° inclination.

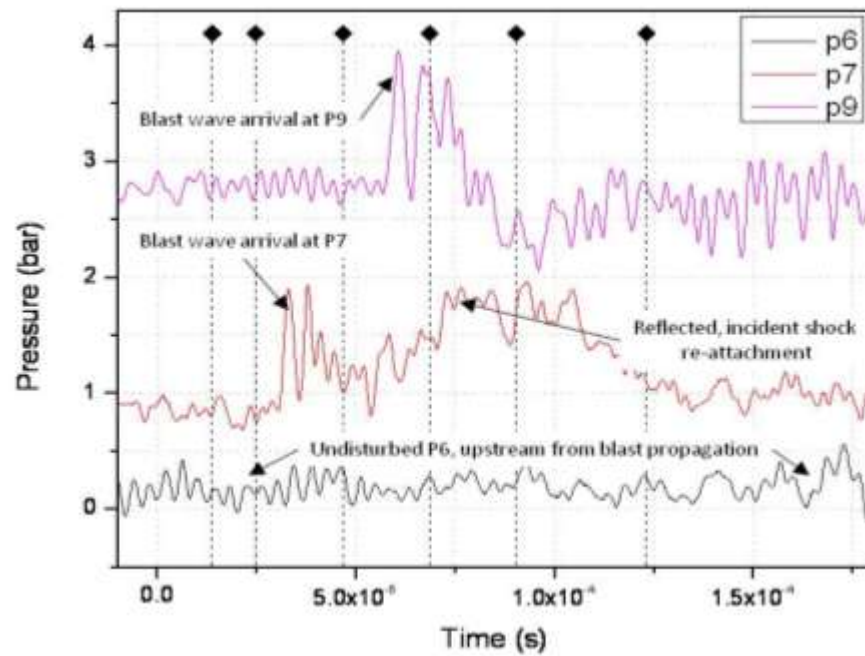


Fig. 21 Run#17 - Measured pressure distribution across shroud under-surface. Traces offset. schlieren frames from Fig. 19 are marked for with diamonds.

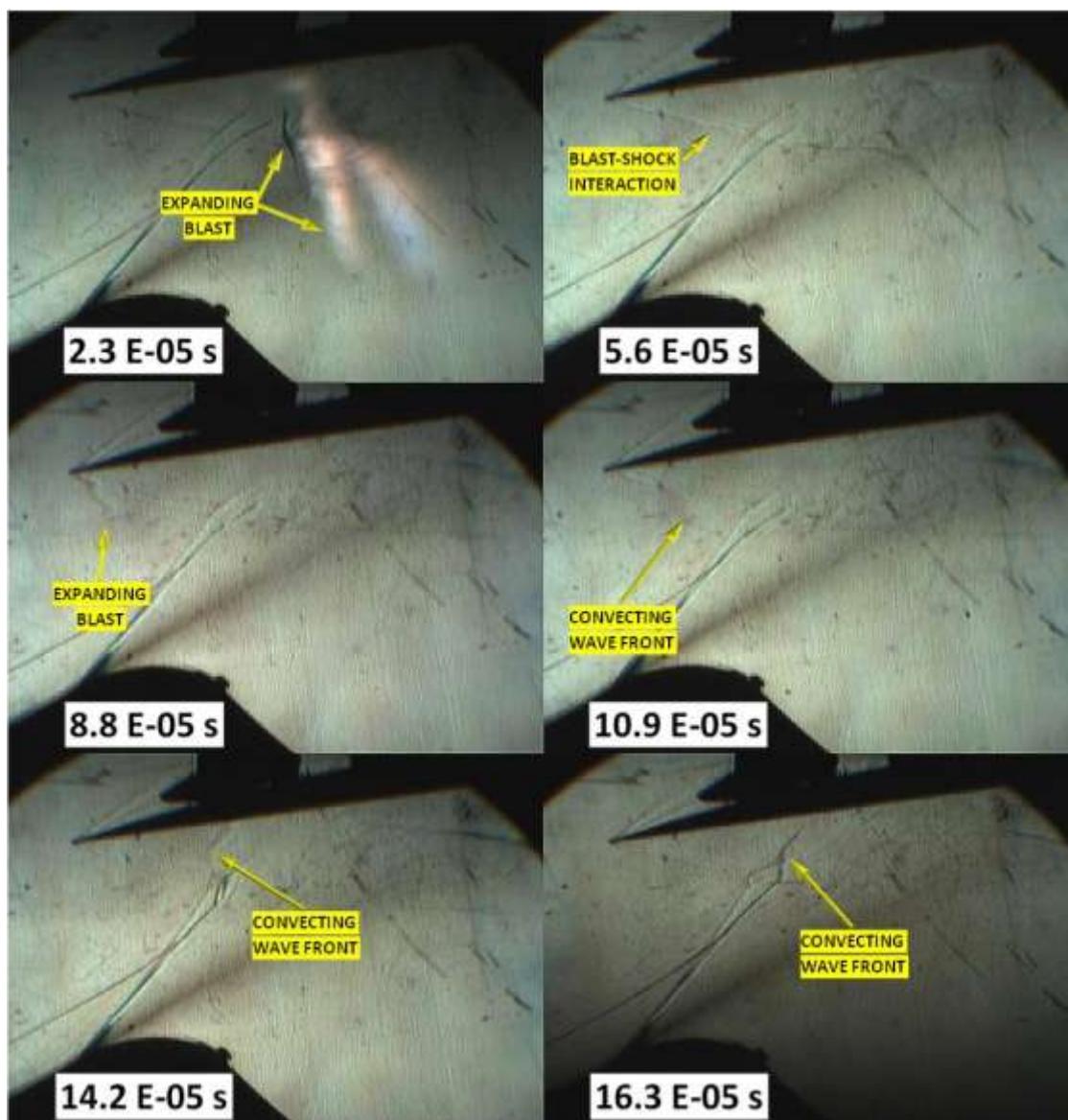


Fig. 22 Run#18 - Laser induced blast wave interaction with oblique shocks and shroud under-surface. Both center body and shroud at -7.5° inclination. ($M=5.94$; $T_\infty=284.4$ K; $P_\infty=4.88$ kPa; $E_p=121\pm 12$ J)

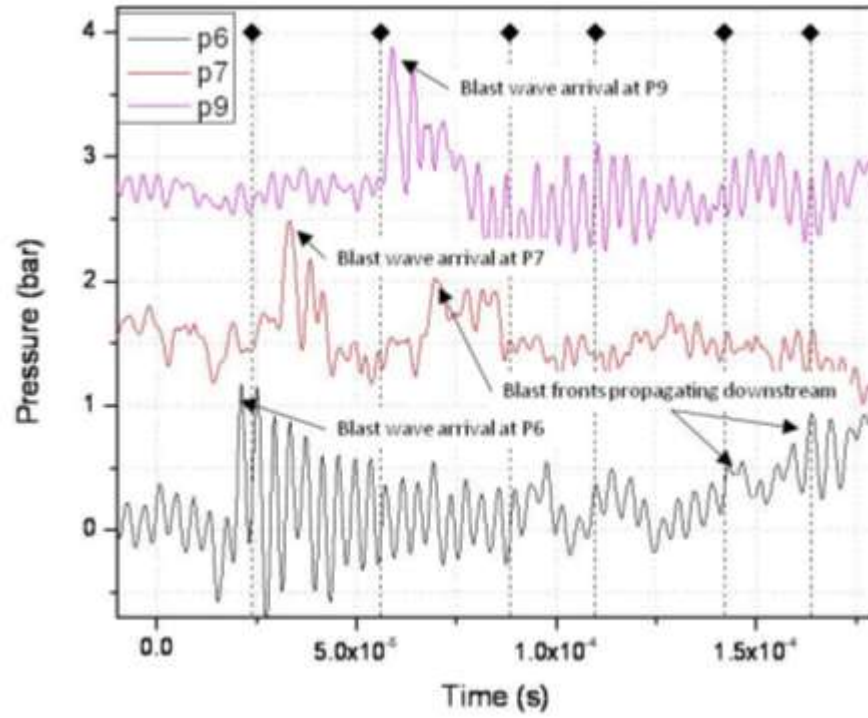


Fig. 23 Run#18 – Measured pressure distribution across shroud under-surface. Traces offset. Schlieren frames from Fig. 22 are marked for with diamonds.

Run 19 was performed at test conditions identical to Run 18, with only a slight difference in the free stream conditions and laser pulse energy (177 ± 18 J). Due to EMI, the schlieren image sequence following laser-induced air-breakdown was lost. The pressure distribution across the under-surface of the shroud is displayed in Fig. 24, along with the photon drag detector trace that provides laser pulse timing.

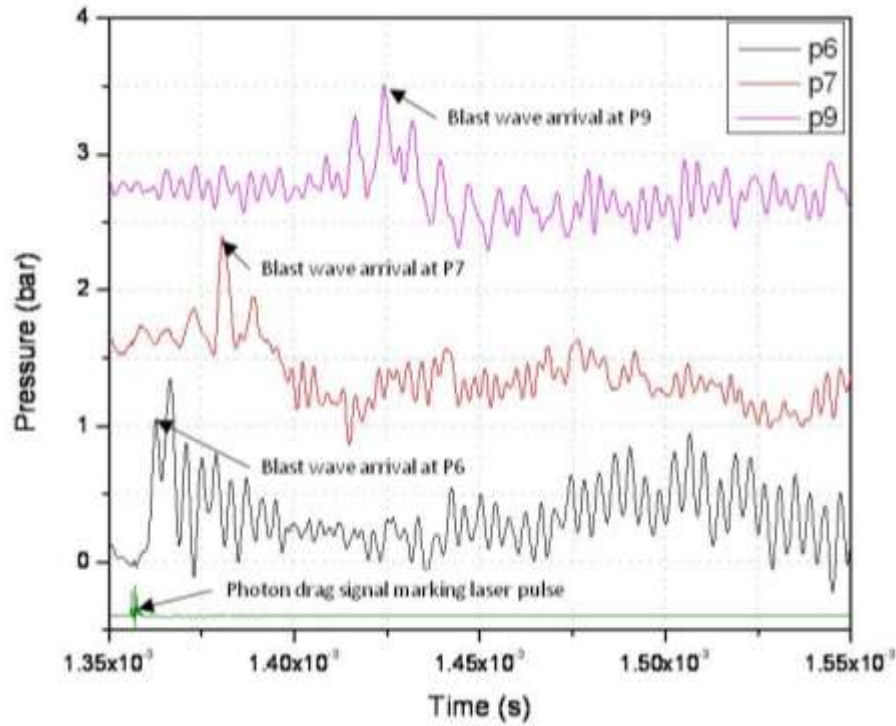


Fig. 24 Run#19 – Measured pressure distribution across shroud under-surface; traces offset. Photon-drag detector signal provides timing for laser pulse delivery.

New HST test conditions were set for the final runs where the free-stream Mach number was increased substantially from the prior series (performed at Mach 5.95), with the same stagnation temperature of about 1850 K. For Run 20, the same 2-D model center body and shroud configuration was retained; both inclined -7.5 degrees (counterclockwise) from horizontal. The T3 test section Mach number was increased from 5.95 to 8.6 simply by changing the nozzle throat insert, with the enthalpy kept unchanged. The lower free stream P_∞ and ρ_∞ produced a noticeable weakening of the shock waves in the schlieren images, which became less visible. Unfortunately during this run, the high-speed schlieren camera triggered too late, capturing only the re-stabilized steady flow—well after the expanding laser-induced blast wave had faded. Such schlieren data loss is still common, despite the progress made in EMI mitigation. On the other hand, good pressure traces were acquired, as displayed in Figs. 25 and 26. Note the expanded timescale shown in Fig. 25 which extends over the entire experiment duration of ~ 1.8 ms, from HST incident shock arrival at the nozzle entrance, through diaphragm rupture and flow establishment in the test section (confirmed by pressure transients), and finally the laser firing and blast-induced mechanical noise. Figure 26 zooms into a 200 μ s long time-window (same as previous runs) that highlights only the shroud sensor pressure signals (P6, P7, P9) following the laser energy deposition. The photon drag detector's trace in Fig. 26 (bottom) gives the laser pulse timing. Note that sensor response to the laser-induced blast and subsequent mechanical noise is similar to that in Runs 1-4: i.e., all signals simultaneously jumped when the laser was fired, and the subsequent pressure

increases (caused by the propagating blast wave) are seen as offset peaks in Fig. 26 – quite in contrast to previous results from Runs 16-19, despite the same geometrical configuration employed.

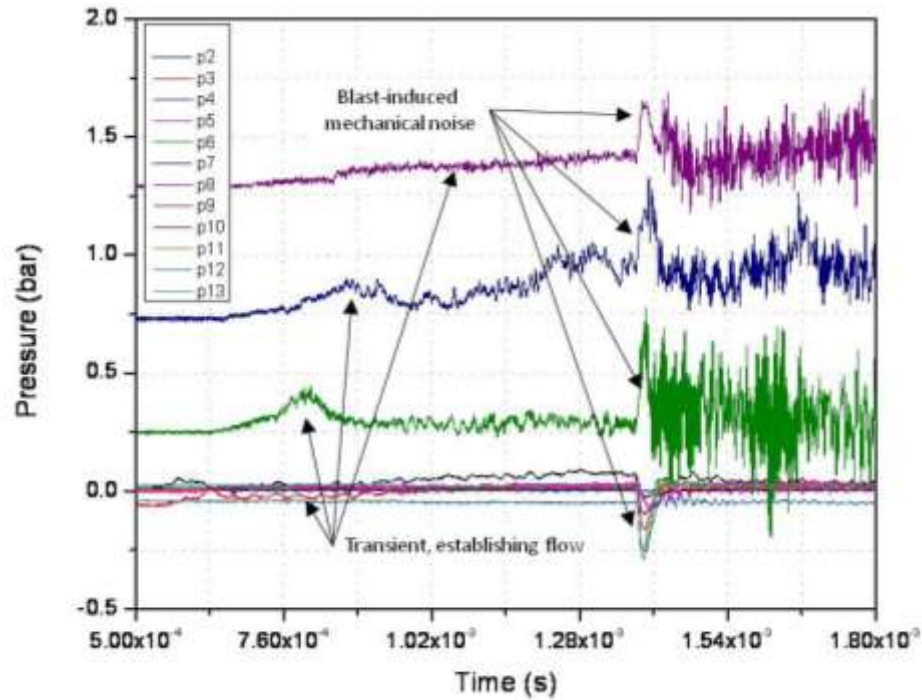


Fig. 25 Run#20 – Extended duration pressure distribution over 2-D model, also showing transients before full flow establishment. Shroud sensors offset for clarification. ($M=8.6$; $T_\infty=128.8\text{K}$; $P_\infty=0.566\text{ kPa}$; $E_p=189\pm20\text{ J}$)

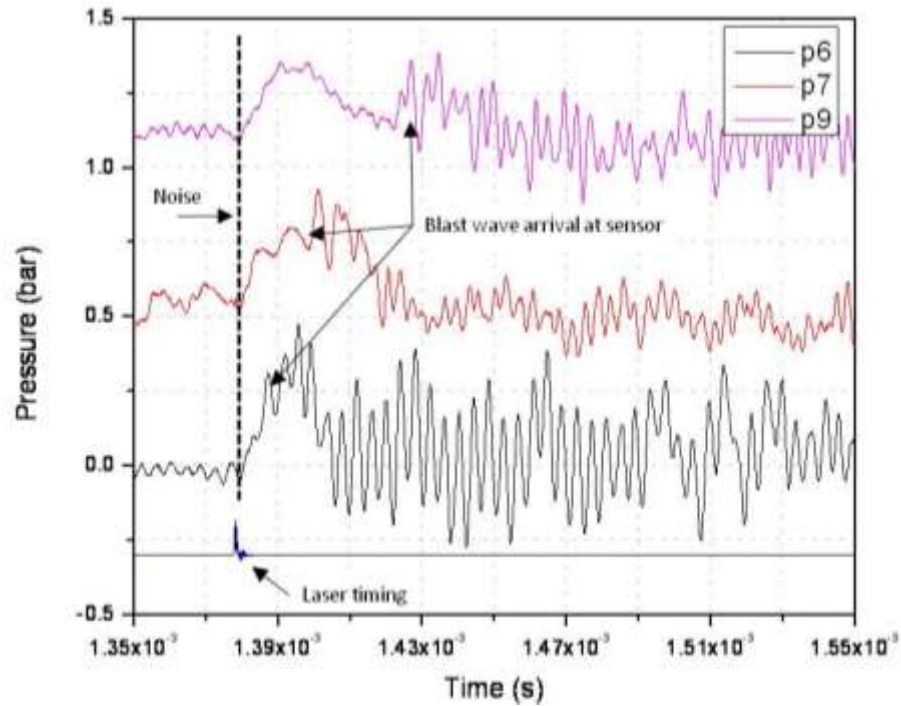


Fig. 26 Run#20 – Pressure distribution over shroud under-surface showing P6, P7, P9 signals, masked by mechanical noise. Photon drag detector signal gives laser pulse timing (bottom trace). Pressure traces offset.

For Runs 21 to 24, the last section of the conical divergent nozzle leading to the test section was re-installed, bringing the exit diameter from 491 mm back up to 610 mm, for a nominal Mach number of 10.0 (calculated equilibrium condition of $M \sim 9.45$). In Run 21 the model/shroud geometry was unchanged from Run 20; the only difference in the test setup being the free stream condition and laser pulse energy of 196 ± 20 s. Notable schlieren and pressure distribution data were obtained, as shown in Figs. 27 and 29. The long exposure photograph in Fig. 28 was also taken during the run, where the unique bifurcated luminous plasma is likely caused by the hollow laser beam emitted from the 620-TEA unstable resonator.

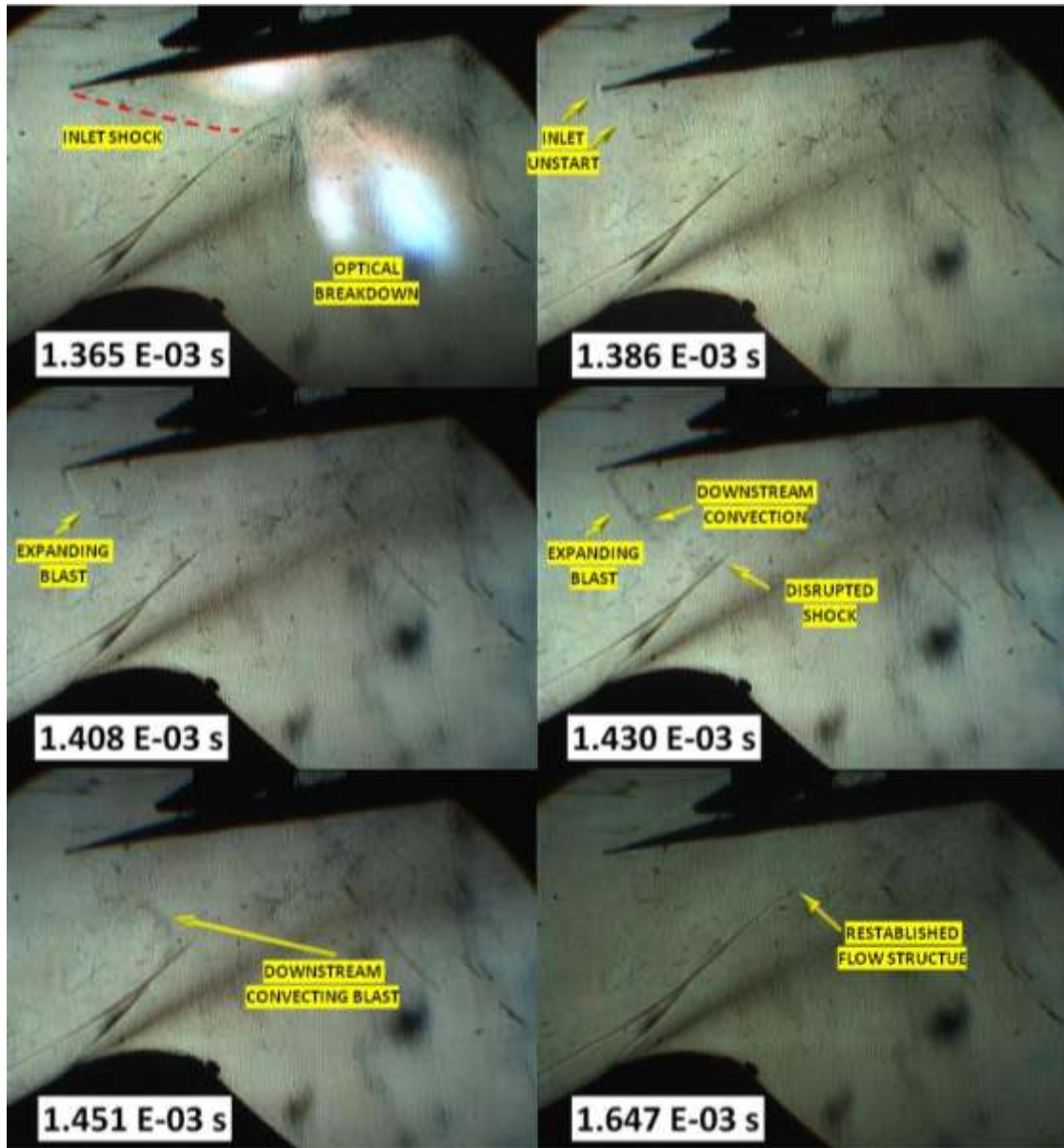


Fig. 27 Run#21 – Laser induced blast wave interaction with oblique inlet shocks and shroud under-surface. Model and shroud at -7.5° inclination. ($M=9.44$, $T_\infty = 108$ K, $P_\infty = 0.301$ kPa, $E_p=196 \pm 20$ J)

Figure 27 also reveals the interaction dynamics for the laser-induced breakdown and blast wave with the established Mach 9.44 flow structure and shroud under-surface. The upper left schlieren image reveals that air-breakdown is triggered in two regions (or lobes) simultaneously: a) a lower bifurcated breakdown centered across the inlet gap; and b) a second surface-induced breakdown initiated at the focal line on the shroud under-surface. The cylindrical blast wave launched from the laser focal line is seen to propagate upstream (against the shroud under-surface) into the region directly behind the weak oblique shock attached to the shroud's leading edge; this causes the inlet to unstart at $22 \pm 4 \mu\text{s}$ after the laser energy deposition, just as this oblique shock detaches from the leading edge. Next, as the expanding blast wave is convected downstream, its interaction with the lower oblique bow shock wave formed off the compression ramp/forebody is clearly visualized. The whole process, from laser-induced breakdown to the restoration of the original flow field takes just $292 \pm 4 \mu\text{s}$.

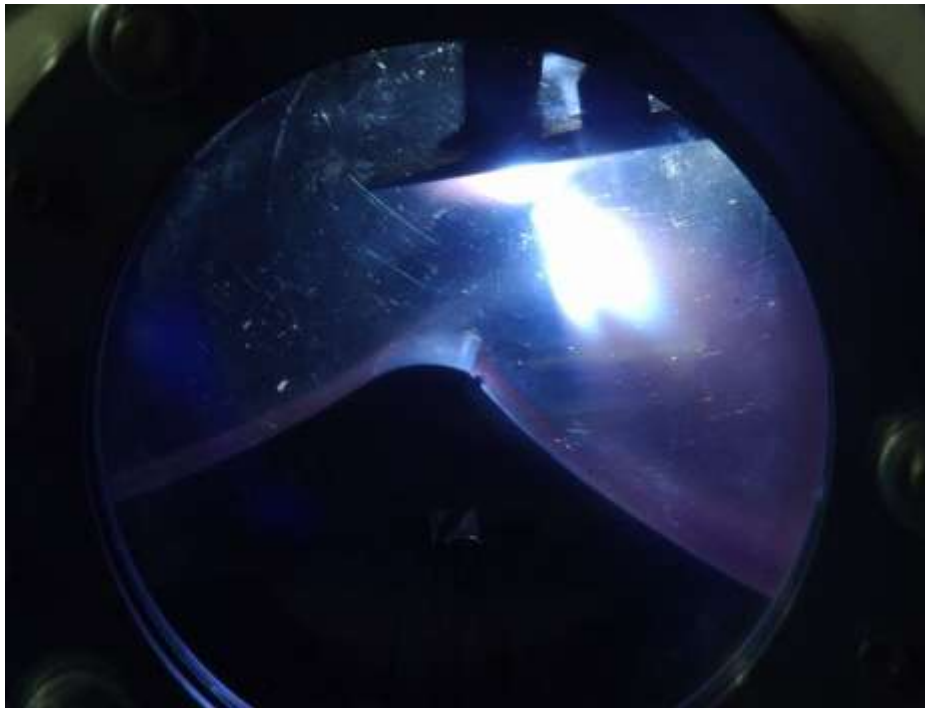


Fig. 28 Run#21 – Long exposure (open shutter) photograph of bifurcated air-breakdown geometry across inlet gap, and secondary breakdown on shroud under-surface.

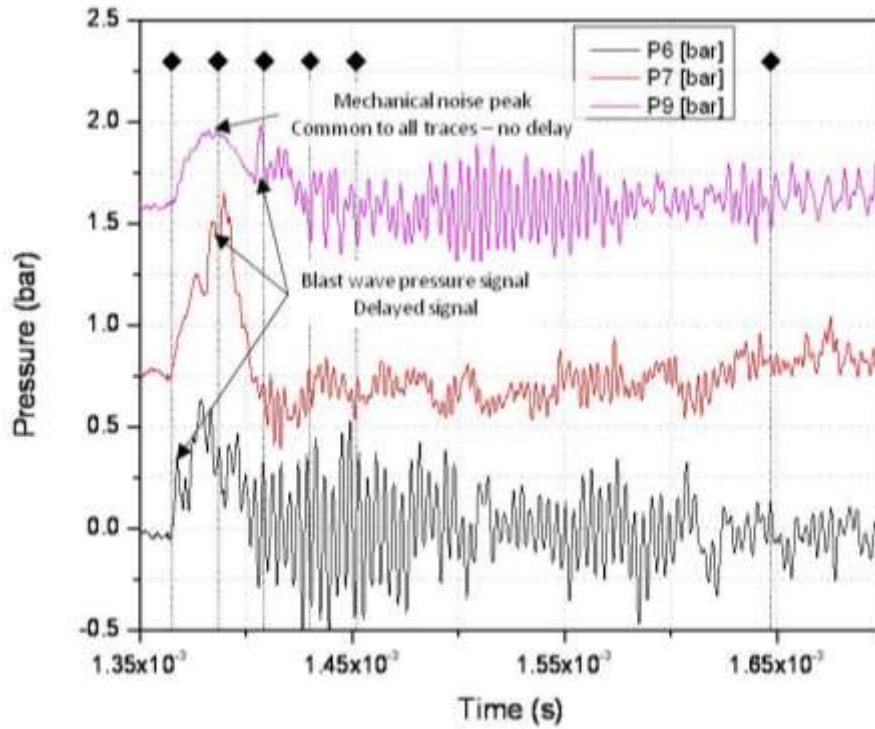


Fig. 29 Run#21 – Measured pressure distribution across shroud under-surface; traces offset. Schlieren frames from Fig. 27 are marked with diamonds.

After correlating dominant phenomena from the schlieren images sequence in Fig. 27 (Run 21), against the sensor traces in Fig. 29, there can be little doubt that the common source of high-frequency mechanical vibration (noise) is due to the timing of laser-induced breakdown at the shroud under-surface—delivering the “hammer” effect, previously discussed. In contrast, the previous runs were performed at higher static pressures, wherein much of the laser energy was deposited across the inlet flow-field at some distance removed from the shroud under-surface—delivering a smoother interaction with reduced noise levels. Due to the excessive noise interference, accurate pressure readings across the shroud under-surface with P6/P7/P9 could not be quantified; only the arrival times for the propagating laser-induced blast wave can be inferred by the small “blips” on the high frequency noise signature.

Prior experience with the present 2-D model proves that shroud pressures can be accurately read only in runs for which no “hammer” effects are present. However, with sophisticated signal processing software, it may be possible to decouple the pressure signals from the noise signatures, but this challenge must await future test campaigns. For the near term, a more promising and immediate solution was already mentioned: i.e., simply install all shroud PCB sensors into vibration-isolating plastic inserts manufactured from a range of materials with different properties, and then through actual HST testing, down-select the ideal choice of insert material on the basis of signal quality.

Runs 22 to 24 were carried out with HST setup conditions identical to Run 21 except that the shroud was pitched even further forward to -24° with respect to horizontal, and its lower surface was placed 1.5 cm below the laser focus. All previous runs had the laser focal line placed coincident with the shroud under-surface to facilitate laser-induced breakdown—i.e., ‘focus-on-shroud’ configuration.

Figure 30 (Run 23) revealed a much weaker laser-induced blast wave on the shroud under-surface than for Run 21. Also, absence of the bifurcated, mid-channel breakdown (seen in Run 21) may be attributed to: a) the low laser pulse energy of 106 ± 11 J, which was lower than usual; and, b) the -24° shroud inclination, which generated an expansion wave off the shroud’s leading edge—that interacted with the shock off the inlet compression ramp and further reduced the local static pressure across the inlet channel/gap.

As in Run 21, the schlieren images sequence in Fig. 30 captures a similar inlet unstart at 22 ± 4 μ s following the air-breakdown for Run 23, driven by the laser-induced blast wave expanding across the shroud under-surface. The duration of the entire event was measured at 114 ± 4 μ s—roughly half that seen in Run 21—again, probably due to the lower local static pressure and weaker laser pulse.

Just prior to Run 22, the faulty sensor P8 was finally replaced with a new PCB unit to enable pressure measurements at *four* positions across the shroud under-surface, as had originally been planned. Figure 31 shows these four traces for Run 23 along with the timing of schlieren frames (shown in Fig. 30), marked with diamond-shaped symbols. Significantly lower pressure increases were registered by passage of the laser-generated blast wave, and the signal magnitudes in Fig. 31 were very near the random noise level, once more due to the reduced local static pressure and laser energy. Also, the “hammer” effect was absent, in large measure due to the low laser pulse energy, and more importantly, because the shroud lower surface was positioned below the laser focal line, resulting in a larger air-breakdown region.

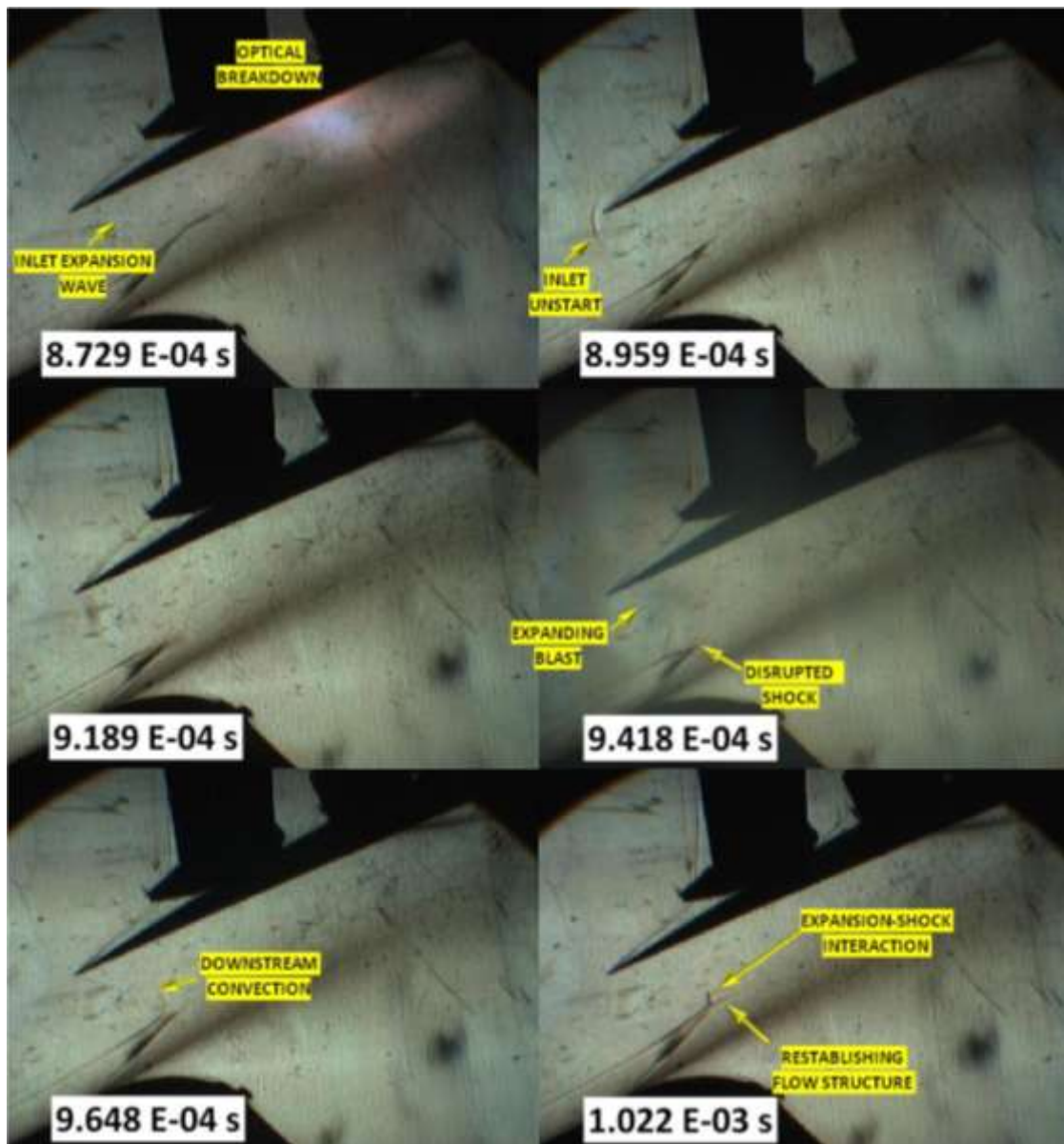


Fig. 30 Run#23 – Laser induced blast wave interaction with oblique shocks and shroud under-surface. Model at - 7.5° and shroud at -24° inclination. ($M=9.43$, $T_\infty=113.7 \text{ K}$, $P_\infty=0.293 \text{ kPa}$, $E_p=106\pm11 \text{ J}$)

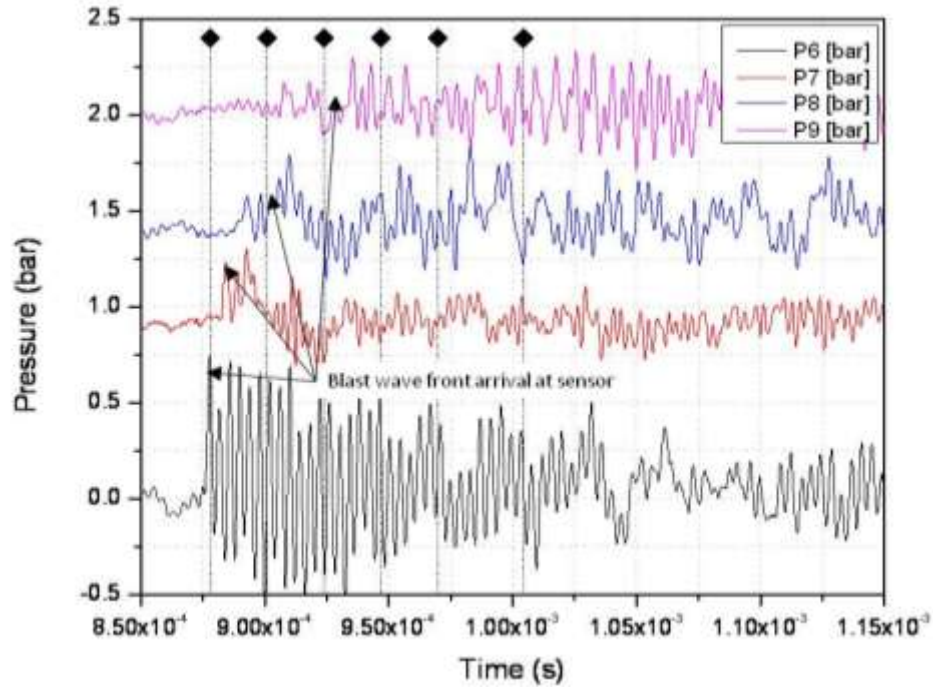


Fig. 31 Run#23 – Measured pressure distribution at shroud under-surface; traces offset. Schlieren frames from Fig. 30 are marked for clarification.

G. Conclusions

The present Phase I research campaign was facilitated through an international collaboration (at top governmental-to-government level) between the United States Air Force and the Brazilian Air Force, and carried out at the Henry T. Nagamatsu Laboratory of Aerothermodynamics and Hypersonics (HTN-LAH) in São Jose dos Campos, Brazil. This IEAv-CTA experimental facility is the first in the world to be set up expressly for Hypersonic Laser Propulsion (LP) research. The HTN-LAH facility comprises the T3 Hypersonic Shock Tunnel (HST), the Lumonics 622-TEA laser system, and dedicated instrumentation. The present two-dimensional LP model—based on the Lightcraft Technology Demonstrator (LTD) concept—was designed, manufactured, and installed into the T3 HST for the present campaign.

Phase I experiments were carried out under static (i.e., quiescent flow) and then hypersonic flow conditions with two principal research objectives in mind: 1) measurement of time-dependent surface pressure distributions subsequent to pulsed laser energy deposition and the resulting laser-induced blast wave expansion through the 2-D model's absorption chamber; and, 2) Schlieren visualization of the evolving flow field and blast wave structures, and their interaction with impulse generating surfaces. The results collected thus far have yielded invaluable insight for the future, Phase 2 hypersonic campaign, as well as useful R&D data for future airbreathing LP engine concepts.

The Lumonics 622-TEA laser system utilized delivered ~200 J pulses into the T3 tunnel for hypersonic airbreathing laser propulsion tests with the 2-D cross section, Lightcraft model. Other than analytical/numerical studies of similar laser ramjet/scramjet geometries, no prior hypersonic investigations of this nature have been reported in the literature. The two principal experimental goals were to: a) measure the time-variant pressure distributions over the model's internal thrust-generating surfaces (i.e., absorption chamber); and, b) capture high speed Schlieren flow field visualizations of the thrust production process -- to reveal the influence of engine geometrical features during blast wave expansion. These Mach 6-10 experiments constitute the first attempt to measure C_m performance from an array of pressure transducers distributed over the model. Such data is important for future LP research in guiding modifications and improvements to the basic engine/vehicle geometry studied here.

The following conclusions were achieved from the Phase I hypersonic campaign:

- The 2-D Lightcraft model (~30 cm focal “radius”) is roughly modeled after a half-scale Lightcraft Technology Demonstrator (LTD); the LTD had a focal ring radius of 60 cm and linear focal energy density (E_{FD}) requirement of 87.5 J/cm at Mach 5 and 30 km altitude; to first order, E_{FD} scales with the focal ring radius so the 2D model needs 43.8 J/cm for optimum performance.
- The 2D hypersonic model has a 135 mm focal line, so ~590 J is needed for optimum impulse generation; at 200 J (single 620-TEA laser charged to 70 kV; unstable resonator mode), the linear focal energy density is 14.8 J/cm or 34% of ideal; doubling E_p to 400 J (622-TEA charged to 70 kV; unstable resonator mode) brings it up to 68%—much closer to optimum;
- Only “off-design” inlet conditions have been tested to date; geometrical similarity was not achieved with the present 2-D engine/vehicle model (awaiting modifications for a future experimental campaign);
- The present 2-D model is prone to “inlet unstart” even at reduced pulse energies; inlet unstart is accentuated with increasing shroud inclination, and sub-ideal internal working fluid properties (static pressure and density);
- Efficient laser impulse generation without inlet unstart requires optimized inlet condition – to be studied in the subsequent campaign;
- Improved Lightcraft inlet designs will permit higher E_p , greater peak engine pressures, and elevated impulse levels;
- Increased blast wave confinement times and reduced working fluid flow speeds (with higher static pressure and density) will enhance impulse delivery in the absorption chamber and plug nozzle;

- The laser-induced air-breakdown geometry (inside the engine) is driven by the parabolic rear-optic focusing geometry upon shroud, but can also be dominated by particulate-induced breakdown triggered off “contaminants” in the T3 hypersonic flow;
- PCB pressure sensor noise levels are very high, and because of the “hammer” effect and excessive ringing, no C_m analysis was possible;
- An analysis of the time-variant pressure distributions and schlieren movies reveals that engine’s air refresh time (or propulsion cycle duration, τ_{cycle}), equates to a maximum PRF of approximately 10 kHz;
- Powered flight at hypersonic speeds is likely feasible, but requires optimum inlet condition, an optimum shroud angle, and other refinements in engine/vehicle geometry; CFD analysis will be needed for optimization;

Developing an airbreathing (i.e., $I_{sp}=\infty$) Lightcraft engine/vehicle is a complex multidisciplinary task for which the difficulty grows with increasing flight Mach number and altitude objectives. As with any innovative/future airbreathing engine, only extensive R&D can reveal the feasible flight operational envelope, but several features unique to laser propulsion must be kept in mind:

With BEP launchers, the overall engine efficiency can be relaxed in favor of *high acceleration* performance, which is in sharp contrast with existing airbreathing chemical propulsion (e.g., hydrogen/hydrocarbon-fueled) designed for *efficient “cruise”* performance. With the latter, a reduction in chemical-fueled scramjet efficiency negatively impacts specific fuel consumption, which dictates larger propellant loads and tankage penalties, higher structural mass fractions, and ultimately, increased fixed and recurrent costs. However with ground-based power-beaming infrastructure, such engine/vehicle liabilities can be transferred to the GBL, where infrastructure capital costs can be amortized over copious launches (e.g., life cycle of 10-20 yrs), with recurring costs limited to maintenance and electric power rates.

From the present hypersonic results, it is obvious that the laser-induced breakdown and time-variant compressible flow-field over a Lightcraft engine/vehicle and through the absorption chamber is an exceedingly complex process. Hence, expedient progress in evolving future Lightcraft engine/vehicle can only be made with a combined numerical/experimental approach. Specialized CFD codes with full-blown chemistry can provide fundamental insight to the plasma physics, but they must be fully calibrated against experimental data—which will take time. Meanwhile, rudimentary insight can be gained with commercial CFD packages that accurately model just the propagating blast waves, using input initial conditions from actual experiments. This approach can enable more detailed analyses of time-variant surface pressure distributions in the absorption chamber, as well as interactions between two sequential blasts within the engine.

In summary, the research work presented herein has paved the way for future investigations into hypersonic airbreathing laser propulsion physics. The present results set an important historical precedent, since prior hypersonic LP research has largely been speculative—limited only to theoretical and numerical studies—and lacking the necessary experimental data to “anchor” such simulations against nature.

5. PERSONNEL ASSOCIATED TO THE PRESENT EFFORT:

Marco Antonio Sala Minucci. Principal Investigator. Also, He is TPO of the Annex no. DEA-AF-05-BR-8803 to the Master Data Exchange Agreement between the United States Department of Defense and the Ministry of Defense of Brazil for Fundamental Mechanisms in Hypersonic Aerodynamics (March 2005);

Paulo Gilberto de Paula Toro. Co-Principal Investigator;

Leik N. Myrabo. Professor at the Rensselaer Polytechnic Institute - RPI, Troy, NY. Ph.D. Thesis Advisor of Israel Irone Salvador.;

Israel Irone Salvador. Ph.D. student at the Rensselaer Polytechnic Institute- RPI, Troy, NY. Co-Principal Investigator;

Antonio Carlos de Oliveira. Senior Scientist at the Institute for Advanced Studies;

José Brosler Channes Júnior. Electronic Engineer at the Institute for Advanced Studies;

Israel da Silveira Rego. Professor at the ABC Federal University- UFABC, São Paulo, Brasil;

David Romanelli Pinto. Undergraduate student; and

Tiago Victor Cordeiro. Undergraduate student.

6. PUBLICATIONS AND PRESENTATIONS:

Salvador, I. I. “Static and Hypersonic Experimental Analysis of Impulse Generation in Air-breathing Laser-Thermal Propulsion,” Ph.D. Dissertation, Mechanical, Aerospace and Nuclear Engineering Dept., Rensselaer Polytechnic Inst., Troy, NY, 2010.

Salvador, I. I., Myrabo, L. N., Minucci, M. A. S., Toro, P. G. P., Oliveira, A. C., Channes, J. B. Jr. and Rego, I. S., “Experimental Analysis of a 2-D Air-Breathing Laser Lightcraft in Static Conditions,” *Journal of Propulsion and Power* (to be published).

Kenoyer, D. A., Salvador, I. I., Myrabo, L. N., Notaro S. S. and Bragulla, P. W., “Experimental Investigation of Axial and Beam-Riding Propulsive Physics with TEA CO₂ Laser,” *2010 International High-Power Laser Ablation Conference*, Santa Fe NM, April, 2010.

Oliveira, A. C., Channes Jr, J. B., Marcos, T. V. C., Pinto, D. R., Vilela, R. G. S., Galvão, V. A. B., Mantovani, A. F., Costa, F. J., Assenção, J. A. S., Santos, A. M., Toro, P. G. P., Minucci, M. A. S., Rego, I. S., Salvador, I. I. and Myrabo, L. N., “Laboratory

Facilities and Measurement Techniques for Beamed-Energy-Propulsion Experiments in Brazil, 7th International Symposium on Beamed Energy Propulsion – ISBEP 2011, Ludwigsburg, Germany, April, 2011.

Salvador, I. I., Myrabo, L. N., Minucci, M. A. S., Oliveira, A. C., Rego, I. S., Toro, P. G. P. and Channes Jr, J. B., “Static and Hypersonic Experimental Analysis of Air-Breathing Laser Thermal Propulsion,” 7th International Symposium on Beamed Energy Propulsion – ISBEP 2011, Ludwigsburg, Germany, April 2011.

Pinto, D. R., Marcos, T. V. C., R., Galvão, V. A. B., Oliveira, A. C., Channes Jr., J. B., Minucci, M. A. S. and Toro, P. G. P., “Flow Characterization of the T3 Hypersonic Shock Tunnel,” 28th International Symposium on Shock Waves – ISSW 2011, Manchester, UK, July 2011.

Minucci, M. A. S. and Toro, P. G. P. “O Brasil e o Futuro do Acesso ao Espaço,” IN Espaço Exterior: Ciência, Tecnologia, Ambiente e Sociedade, Ricco, M. F. F., Funari, P. A. and Carvalho, A. V., Editors, Editora Habilis, Erechim, RS, Brasil, 2011, ISBN 978-85-60967-38-4.

7. INTERACTIONS/TRANSITIONS: None.

8. NEW DISCOVERIES, INVENTIONS, OR PATENT DISCLOSURES: None.

9. HONORS/AWARDS: None.